Riemann-Silberstein geometric phase in 4D polarization space

Yuqiong Cheng,[1, *] Yuan-Song Zeng,[2, 3, *] Wanyue Xiao,[1] Tong Fu,[1]
Jiajun Wu,[2] Geng-Bo Wu,[2, 3, †] Din Ping Tsai,[1, 2, 3, ‡] and Shubo Wang[1, §]

[1]*Department of Physics, City University of Hong Kong, Kowloon, Hong Kong, China*
[2]*Department of Electrical Engineering, City University of Hong Kong, Kowloon, Hong Kong, China*
[3]*State Key Laboratory of Terahertz and Millimeter Waves,*
City University of Hong Kong, Kowloon, Hong Kong, China
(Dated: November 18, 2025)

Geometric phase is a far-reaching concept in quantum and classical physics. The first discovered geometric phase, the Pancharatnam-Berry (PB) phase, has profoundly shaped nanophotonics through metasurfaces. However, the PB phase arises from SU(2) polarization evolution and is constrained to a 2D polarization space, failing to capture the full polarization degrees of freedom. We generalize geometric phase to the 4D Riemann-Silberstein (RS) space that simultaneously describes electric, magnetic, and hybrid electric-magnetic polarizations. We show that SU(4) polarization evolution can generate a new geometric phase, the RS phase, alongside the PB phase. Unlike the PB phase that typically manifests in circularly polarized light, the RS phase can emerge in arbitrarily polarized light. Together, they enable a high-dimensional geometric framework for light propagation across general interfaces. We reveal that the phase shifts governed by Fresnel equations are direct manifestations of the RS-space geometric phases, integrating a century-old wave theory into this paradigm. We experimentally validate the framework using metasurfaces and achieve high-dimensional wavefront manipulation. Our work offers fundamental insights into the geometric nature of light-matter interactions, with implications for topological and non-Abelian physics in classical wave systems.

Introduction

Geometric phases emerge from state evolution in parameter space and provide a unified framework for understanding diverse phenomena in quantum and classical physics [1–4]. These phases have been extensively studied in various physical systems, including quantum particles [2, 5–7], condensed matter [8, 9], and classical wave systems [10–14]. In optics, geometric phases can give rise to intriguing phenomena such as spin-orbit interactions [15] and photonic topological states [16–19], providing important insights into the geometric and topological properties of optical fields [20–22] and enabling novel mechanisms for light manipulation [23–28].

The PB phase has recently attracted significant attention for its crucial role in topological meta-optics and structured light manipulation [29–37]. This phase arises from SU(2) evolution of electric polarization on the Poincaré sphere [38, 39], which is a 2D space describing the polarization of a two-component spinor. However, light is an electromagnetic wave comprising an electric field **E** and a magnetic field **H**, which can be described as a bispinor in the Dirac-like formulations of Maxwell's equations [40, 41]. For monochromatic waves, both **E** and **H** are two-component vector fields within the local frame defined by their polarization ellipses [20, 42], and their polarizations can be different. Consequently, the complete polarization state of a monochromatic electromagnetic wave resides in a 4D Hilbert space (i.e., direct sum of electric and magnetic polarization spaces), termed RS space in this paper, which simultaneously characterizes electric, magnetic, and hybrid electric-magnetic polarizations. The SU(4) evolution of the 4D complete polarization can give rise to nontrivial geometric phases beyond the conventional PB phase, which have thus far remained elusive. These RS-space geometric phases are essential to establishing a unified geometric framework for light-matter interactions involving complex materials or structured light.

In this work, we expand the geometric phase paradigm from the 2D polarization space to the 4D polarization space. We identify a new class of geometric phase, the RS phase, which can emerge in general electromagnetic waves and is governed by the hybrid electric-magnetic polarization, in contrast to the conventional PB phase associated with individual electric (magnetic) polarization. The RS and PB phases complement each other, and together enable a high-dimensional geometric framework for light propagation across general interfaces. This framework reveals a hidden geometric nature of the phase shifts due to light transmission and reflection at interfaces, a classical phenomenon governed by Fresnel equations. We experimentally demonstrate the RS phase and verify the framework at microwave frequencies using metasurfaces, which gives rise to high-dimensional wavefront deflection that cannot be achieved in

* These authors contributed equally.
† bogwu2@cityu.edu.hk
‡ dptsai@cityu.edu.hk
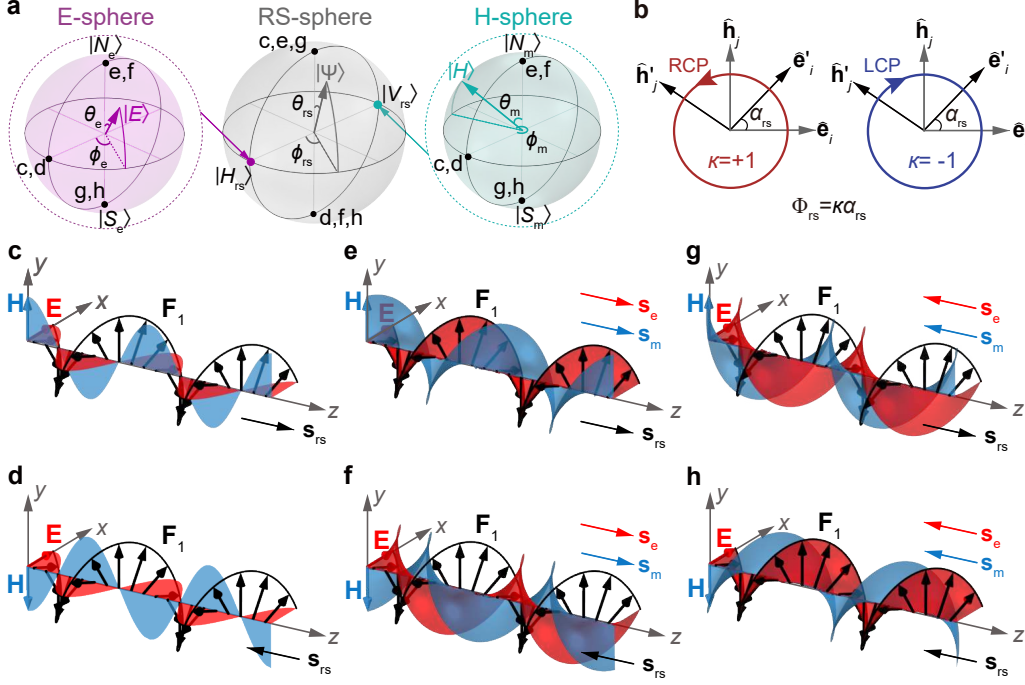§ shubwang@cityu.edu.hk

FIG. 1. **Complete 4D polarization of electromagnetic fields**. (a) Poincaré hypersphere representation of 4D electromagnetic polarization, where the points "c-h" represent the polarizations of the plane waves in the panels (c-h), respectively. (b) RS geometric phase induced by the rotation of the local constitutive frame. Electric field (in red), magnetic field (in blue), and hybrid RS field (in black) of (c) $+z$-propagating linearly polarized plane wave, (d) $-z$-propagating linearly polarized plane wave, (e) $+z$-propagating RCP plane wave, (f) $-z$-propagating RCP plane wave, (g) $+z$-propagating LCP plane wave, and (h) $-z$-propagating LCP plane wave. The electric spin density $\mathbf{s}_\mathrm{e}$, magnetic spin density $\mathbf{s}_\mathrm{m}$, and RS spin density $\mathbf{s}_\mathrm{rs}$ are denoted by the red, blue, and black arrows, respectively.

conventional metasurface systems. The results provide new insights into light-matter interactions at interfaces and expand the toolkit for exploring geometric and topological properties of light.

Geometric phases in RS space

The polarization state of light is conventionally described as a two-component spinor governed by an effective Hamiltonian $\hat{\mathcal{H}} = \hat{\rho} - \frac{1}{2}\hat{\mathrm{I}}_2 = \frac{1}{2}\mathbf{S} \cdot \hat{\boldsymbol{\sigma}}$, where $\hat{\rho} = |E\rangle\langle E|$ is the polarization projector, $\hat{\mathrm{I}}_2$ is the 2×2 identity matrix, $\hat{\boldsymbol{\sigma}}$ is the vector of Pauli spin matrices, and $\mathbf{S}$ is the Stokes vector [38]. The 2D polarization state $|E\rangle$ can be represented on the Poincaré sphere [1]. In our framework, a monochromatic electromagnetic field is described by the wavefuntion $\boldsymbol{\Psi} = \mathbf{E} + i\mathbf{H}$ (Gaussian units are used throughout the paper), as in the Dirac-like formulation of electromagnetism [43]. Here, $\mathbf{E}(\mathbf{r}, t) = E_i(\mathbf{r}, t)\hat{\mathbf{e}}_i + E_j(\mathbf{r}, t)\hat{\mathbf{e}}_j$ is the complex electric field in the local frame with bases $(\hat{\mathbf{e}}_i, \hat{\mathbf{e}}_j)$, and $\mathbf{H}(\mathbf{r}, t) = H_i(\mathbf{r}, t)\hat{\mathbf{h}}_i + H_j(\mathbf{r}, t)\hat{\mathbf{h}}_j$ is the complex magnetic field in the local frame with bases $(\hat{\mathbf{h}}_i, \hat{\mathbf{h}}_j)$. The complete polarization state $|\Psi\rangle$ is a four-component bispinor governed by the effective Hamiltonian $\hat{\mathcal{H}} = \hat{\rho} - \frac{1}{4}\hat{\mathrm{I}}_4 = \frac{1}{2}\mathbf{S} \cdot \hat{\boldsymbol{\lambda}}$, where $\hat{\rho} = |\Psi\rangle\langle\Psi|$ and $\hat{\boldsymbol{\lambda}}$ is the generalized Gell-Mann matrices (Supplementary Note I). This 4D polarization state exhibits both internal polarizations (i.e., the polarizations of individual $\mathbf{E}$ and $\mathbf{H}$ fields) and external polarization (i.e., the hybrid $\mathbf{E}$-$\mathbf{H}$ polarization). It resides in a 4D RS Hilbert space and can be represented on a Poincaré hypersphere [44, 45], as illustrated in Fig. 1a, which comprises three nested Poincaré spheres: E-sphere characterizing the $\mathbf{E}$ field polarization, H-sphere characterizing the $\mathbf{H}$ field polarization, and RS-sphere characterizing the hybrid $\mathbf{E}$-$\mathbf{H}$ polarization. The E-sphere has the north pole state $|N_\mathrm{e}\rangle$ corresponding to right-handed circularly-polarized (RCP) electric field and the south pole state $|S_\mathrm{e}\rangle$ corresponding to left-handed circularly-polarized (LCP) electric field; The H-sphere has the north pole state $|N_\mathrm{m}\rangle$ corresponding to RCP magnetic field and the south pole state $|S_\mathrm{m}\rangle$ corresponding to the LCP magnetic field. Any other point on the E-sphere or H-sphere denotes a SU(2) superposition state parameterized by the polar angle $\theta_\mathrm{e,m}$ and azimuthal angle $\phi_\mathrm{e,m}$. Notably, the RS-sphere characterizes the relationship between E-sphere and H-sphere with θ_rs and ϕ_rs; its horizontal basis state $|H_\mathrm{rs}\rangle$ corresponds to an arbitrary state on the E-sphere; its vertical basis state $|V_\mathrm{rs}\rangle$ corresponds to an arbitrary state on the H-sphere. Any other point on the RS-sphere denotes a SU(4) superposition state $|\Psi\rangle$ (see Methods). The SU(4) evolution of $|\Psi\rangle$ will generally trace out trajectories on all the three spheres, and each sphere with an effective magnetic monopole in the

center will contribute to the total geometric phase of $\mathbf{\Psi}$ with a weighting. In particular, the polarization evolution on the RS-sphere will generate a new type of geometric phase, termed RS phase, which will be elaborated with concrete examples below.

In the following, we will focus on paraxial waves involving transverse electric and magnetic fields that are mutually perpendicular. In such cases, $\mathbf{E}$ and $\mathbf{H}$ exhibit the same polarization, and $\mathbf{\Psi}$ can be decomposed into a pair of orthogonal RS vectors: $\mathbf{\Psi} = \mathbf{F}_1 + \mathbf{F}_2$, where $\mathbf{F}_1(\mathbf{r}, t) = E_i(\mathbf{r}, t)\hat{\mathbf{e}}_i + iH_j(\mathbf{r}, t)\hat{\mathbf{h}}_j$ and $\mathbf{F}_2(\mathbf{r}, t) = E_j(\mathbf{r}, t)\hat{\mathbf{e}}_j + iH_i(\mathbf{r}, t)\hat{\mathbf{h}}_i$. Consequently, the hybrid $\mathbf{E}$-$\mathbf{H}$ polarization reduces to the polarizations of $\mathbf{F}_1$ and $\mathbf{F}_2$. We note that the RS vectors $\mathbf{F}_1$ and $\mathbf{F}_2$ are composed of *complex* electric and magnetic fields, which are different from the conventional RS vector comprising *real* electric and magnetic fields [46–50].

We use electromagnetic plane waves as an example to illustrate the 4D polarization and its representation on the Poincaré hypersphere. We first consider a plane wave with linearly polarized electric and magnetic fields: $\mathbf{\Psi} = (\hat{\mathbf{e}}_x + i\kappa\hat{\mathbf{h}}_y)Ee^{i\kappa k_0 z - i\omega t}$, where $\kappa = \pm 1$ denotes the sign of the propagation direction relative to $+z$ axis. Figures 1**c** and 1**d** show the instantaneous $\mathbf{E}$, $\mathbf{H}$, and $\mathbf{F}_1$ fields for $\kappa = 1$ and $\kappa = -1$, respectively. The polarizations of $\mathbf{E}$ and $\mathbf{H}$ fields are represented by points "c" and "d" on the E-sphere and H-sphere in Fig. 1**a**. The RS field $\mathbf{F}_1$ is RCP for $\kappa = 1$ and LCP for $\kappa = -1$, which are represented by points "c" and "d" on the RS-sphere in Fig. 1**a**. Naturally, we can introduce an RS spin density $\mathbf{s}_{rs} = \frac{1}{16\pi\omega} \text{Im}\left[\mathbf{F}_1^* \times \mathbf{F}_1\right] = \frac{1}{\omega c}\mathbf{P}$, where $\mathbf{P} = \frac{c}{8\pi} \text{Re}\left[\mathbf{E}^* \times \mathbf{H}\right]$ is the time-averaged Poynting vector. This RS spin originates from the intrinsic chirality of RS fields with the handedness defined by $\kappa = \pm 1$.

We further consider a plane wave with circularly polarized electric and magnetic fields: $\mathbf{\Psi} = [(\hat{\mathbf{e}}_x + i\sigma_e\hat{\mathbf{e}}_y) + i\kappa(\hat{\mathbf{h}}_y - i\sigma_m\hat{\mathbf{h}}_x)]Ee^{i\kappa k_0 z - i\omega t}$, where $\sigma_e = \pm 1$ denotes the electric spin, $\sigma_m = \pm 1$ denotes the magnetic spin, and $\kappa = \pm 1$ denotes the RS spin. Note that $\sigma_e = \sigma_m$ for plane waves. The total spin density can be expressed as $\mathbf{s} = \frac{1}{16\pi\omega} \text{Im}\left[\mathbf{\Psi}^* \times \mathbf{\Psi}\right] = \mathbf{s}_e + \mathbf{s}_m + \mathbf{s}_{rs}$, where $\mathbf{s}_e = \frac{1}{16\pi\omega} \text{Im}\left[\mathbf{E}^* \times \mathbf{E}\right]$ is the electric spin density, $\mathbf{s}_m = \frac{1}{16\pi\omega} \text{Im}\left[\mathbf{H}^* \times \mathbf{H}\right]$ is the magnetic spin density, and $\mathbf{s}_{rs} = \frac{1}{16\pi\omega} \text{Im}\left[\mathbf{F}_1^* \times \mathbf{F}_1\right] + \frac{1}{16\pi\omega} \text{Im}\left[\mathbf{F}_2^* \times \mathbf{F}_2\right] = \frac{1}{\omega c}\mathbf{P}$ is the RS spin density. Notably, the sum of $\mathbf{s}_e$ and $\mathbf{s}_m$ corresponds to the conventional optical spin density that has been extensively studied in recent years [15, 51–56], while the RS spin density $\mathbf{s}_{rs}$ has been largely overlooked [50, 57]. Figure 1**e-h** shows the instantaneous $\mathbf{E}$, $\mathbf{H}$, $\mathbf{F}_1$, and spin directions for the plane waves with $(\sigma_e, \sigma_m, \kappa) = (+1, +1, +1), (+1, +1, -1), (-1, -1, +1)$, and $(-1, -1, -1)$, respectively. Their 4D polarizations are represented on the Poincaré hypersphere in Fig. 1**a** as the points "e", "f", "g", and "h", respectively.

The evolution of 4D polarization state $|\Psi\rangle$ simultaneously traces out paths on the E-sphere, H-sphere, and RS-sphere. The electric (magnetic) polarization evolution can generate the PB phase Φ_{pb}, which is proportional to the solid angle subtended by the area enclosed by the evolution path on E-sphere (H-sphere) [1]. Notably, the electric and magnetic polarization evolutions are intrinsically linked through the Maxwell equations. For the considered paraxial waves, the electric and magnetic polarization evolutions trace the same path and contribute to the same PB phase. Additionally, the polarization evolution of $\mathbf{F}_{1,2}$ will generate the RS phase Φ_{rs}, which is proportional to the solid angle subtended by the area enclosed by the evolution path on the RS-sphere (Supplementary Note III). Importantly, Φ_{rs} is independent of Φ_{pb} because Φ_{pb} manifests in the basis states $|H_{rs}\rangle$ and $|V_{rs}\rangle$. Therefore, the total geometric phase due to 4D polarization evolution is $\Phi_{tot} = \Phi_{pb} + \Phi_{rs}$.

The PB phase can be attributed to the coupling between electric (magnetic) spin and rotation of local coordinate frame, where the frame rotation induces a phase variation of the circularly polarized electric (magnetic) field [15]. Similarly, the RS phase can be attributed to the coupling between RS spin and rotation of local *constitutive* frame $(\hat{\mathbf{e}}_i, \hat{\mathbf{h}}_j)$[or $(\hat{\mathbf{e}}_j, \hat{\mathbf{h}}_i)$], as shown in Fig. 1**b**. A rotation of the constitutive frame by angle α_{rs} leads to the transformation of the circularly polarized RS vector: $\mathbf{F}_{1,2} \to e^{i\kappa\alpha_{rs}}\mathbf{F}_{1,2}$. The phase $\kappa\alpha_{rs}$ corresponds to the RS geometric phase, which is proportional to the RS spin κ and the rotation angle α_{rs} of the local constitutive frame.

RS phase at interfaces

The RS phase can emerge in light transmission and reflection at an interface due to 4D polarization evolution, which is determined by the eigen polarization states of the two media forming the interface. Remarkably, the RS phase reveals the hidden geometric nature of the phase shifts governed by Fresnel equations, a cornerstone of classical optics. As shown in Fig. 2**a**, we consider that a plane wave propagates along $+z$ direction and normally impinges on the surface of an isotropic medium with permittivity ε and permeability μ, giving rise to RS polarization evolution. The incident electric (magnetic) field is linearly polarized in x (y) direction. We denote the RS polarization states of the incident, reflected, and transmitted waves as $\left|F_1^{in}\right\rangle$, $\left|F_1^{ref}\right\rangle$, and $|F_1^{tra}\rangle$, respectively. The transmission involves the polarization evolution $\left|F_1^{in}\right\rangle \to |F_1^{tra}\rangle$, while the reflection involves the polarization evolution $\left|F_1^{in}\right\rangle \to |F_1^{tra}\rangle \to \left|F_1^{ref}\right\rangle$. These RS polarization evolutions induce the RS phases Φ_{rs}^{tra} and Φ_{rs}^{ref}, which manifest in the transmitted and reflected waves, respectively. As an example, we assume the medium is a lossless metal. In this case, $\left|F_1^{in}\right\rangle = \frac{1}{\sqrt{2}}(\hat{\mathbf{e}}_x + i\hat{\mathbf{h}}_y), \left|F_1^{ref}\right\rangle = \frac{1}{\sqrt{2}}(\hat{\mathbf{e}}_x - i\hat{\mathbf{h}}_y)$, and $|F_1^{tra}\rangle = \frac{\sqrt{|\mu|}}{\sqrt{|\mu|+|\varepsilon|}}(\hat{\mathbf{e}}_x + \frac{i\sqrt{\varepsilon}}{\sqrt{\mu}}\hat{\mathbf{h}}_y)$. Notably, $|F_1^{tra}\rangle$ is linearly polarized in the constitutive frame with
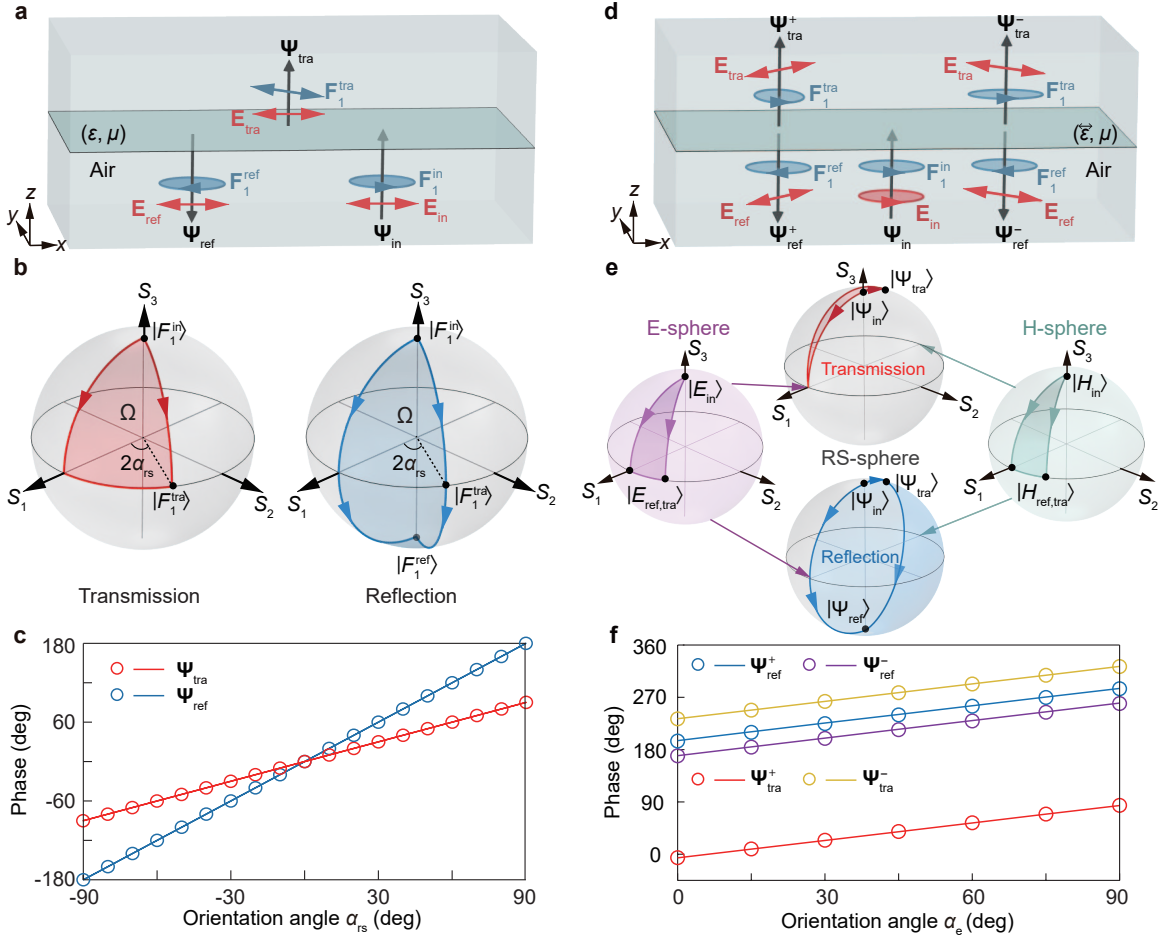
FIG. 2. **RS geometric phase at interfaces**. (a) A plane wave with linearly polarized electric and magnetic fields impinges on an interface of isotropic media, where the RS polarization (blue arrows) undergoes evolutions but electric polarization (red arrows) remains unchanged. (b) Representation of the RS polarization evolution on the RS-sphere for the wave transmission and reflection. We choose the point on S_1 axis as the reference polarization. (c) Transmission and reflection phases for different orientation angles of the transmitted RS polarization. The circles denote the RS geometric phase. (d) A plane wave with circularly polarized electric and magnetic fields impinges on an interface of anisotropic media, where both the electric polarization (red arrows) and the RS polarization (blue arrows) undergo evolutions. (e) Representation of the 4D polarization evolution on the Poincaré hypersphere for the wave transmission and reflection. (f) Transmission and reflection phases for different orientation angle of the electric polarization. The circles denote the total geometric phase.

orientation angle $\alpha_{\rm rs} = \arctan(\frac{{\rm i}\sqrt{\varepsilon}}{\sqrt{\mu}})$, which locates on the equator of the RS-sphere with azimuthal angle $\phi_{\rm rs} = 2\alpha_{\rm rs}$. Thus, changing the material properties (ε, μ) leads to rotation of local constitutive frame and thus the variation of $\phi_{\rm rs}$. Figure 2b shows the polarization evolution paths on the RS-sphere for the transmission and reflection. We calculate the RS phases $\Phi_{\rm rs}^{\rm tra}$ and $\Phi_{\rm rs}^{\rm ref}$ by evaluating the solid angles Ω enclosed by the paths. The results are shown as the circles in Fig. 2c for different orientation angle $\alpha_{\rm rs}$, which agree with the transmission and reflection phases (solid lines) predicted by the Fresnel equations [58]. This relationship holds for normal incidence at general interfaces between isotropic media (Supplementary Note IV).

Both the PB and RS phases can emerge at an interface involving anisotropic media. We consider the interface between air and a non-magnetic medium that has anisotropic in-plane permittivity $\overleftrightarrow{\varepsilon}$ with elements $\varepsilon_{xx} = \varepsilon + \delta\cos\phi, \varepsilon_{yy} = \varepsilon - \delta\cos\phi, \varepsilon_{xy} = \delta\sin\phi e^{-{\rm i}\theta}$, and $\varepsilon_{yx} = \delta\sin\phi e^{{\rm i}\theta}$. The medium supports two orthogonal 4D eigen polarization states. As shown in Fig. 2d, under the normal incidence of a plane wave with polarization $|\Psi_{\rm in}\rangle = \frac{1}{2}[(\hat{\bf e}_x + {\rm i}\hat{\bf e}_y) + {\rm i}(\hat{\bf h}_y - {\rm i}\hat{\bf h}_x)]$, two transmitted waves $|\Psi_{\rm tra}^{\pm}\rangle = \frac{1}{\sqrt{1+|\varepsilon\pm\delta|}}({\bf E}_{\pm} + {\rm i}\sqrt{\varepsilon\pm\delta}{\bf H}_{\pm})$ and two reflected waves $|\Psi_{\rm ref}^{\pm}\rangle = \frac{1}{\sqrt{2}}({\bf E}_{\pm} - {\rm i}{\bf H}_{\pm})$ emerge, where ${\bf E}_+ = \cos\frac{\phi}{2}\hat{\bf e}_x + \sin\frac{\phi}{2}e^{{\rm i}\theta}\hat{\bf e}_y, {\bf E}_- = \sin\frac{\phi}{2}e^{-{\rm i}\theta}\hat{\bf e}_x - \cos\frac{\phi}{2}\hat{\bf e}_y, {\bf H}_+ = \cos\frac{\phi}{2}\hat{\bf h}_y - \sin\frac{\phi}{2}e^{{\rm i}\theta}\hat{\bf h}_x$, and ${\bf H}_- = \sin\frac{\phi}{2}e^{-{\rm i}\theta}\hat{\bf h}_y + \cos\frac{\phi}{2}\hat{\bf h}_x$. Correspondingly, four polarization evolutions occur at the interface:
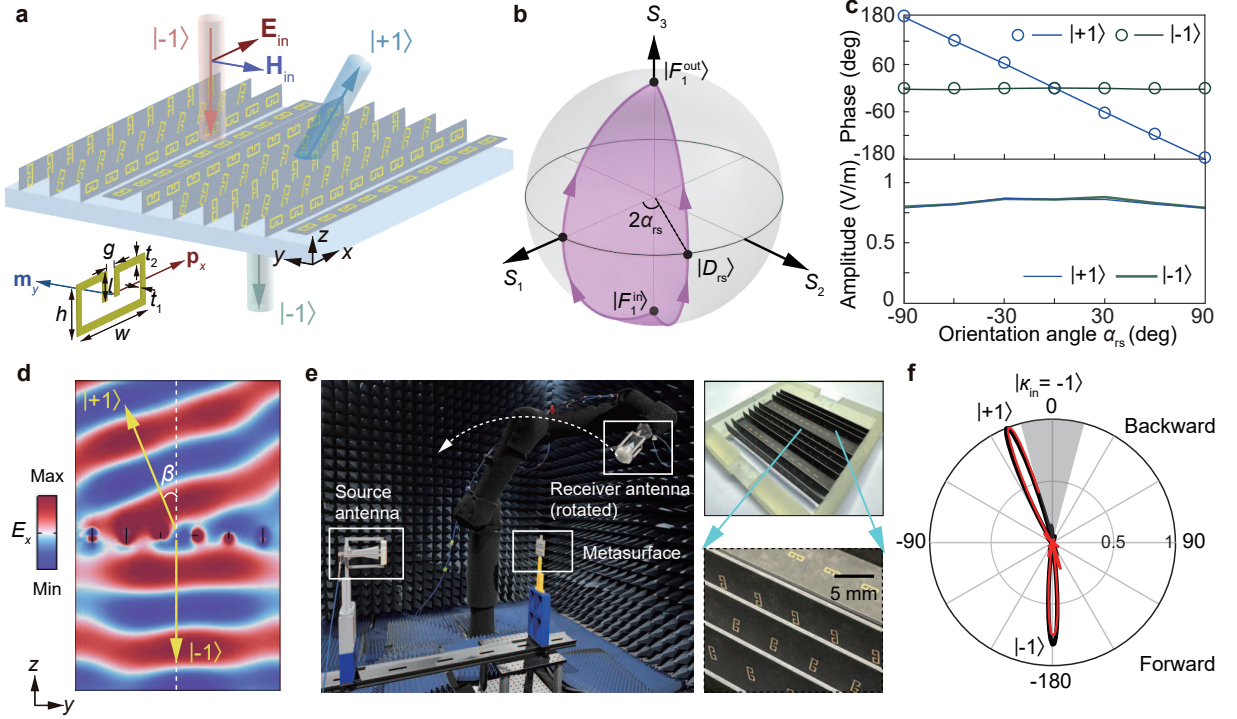
FIG. 3. **RS geometric phase at a metasurface**. (a) Schematic of the RS metasurface under the normally incident plane wave with linearly polarized electric field. The inset shows the structure of the meta-atom. (b) RS polarization evolution on the RS-sphere induced by the metasurface. (c) Theoretical RS geometric phase (symbols), simulated phase (solid lines), and simulated amplitude for the forward and backward scattering fields as a function of the orientation angle α_{rs} of the RS dipole. (d) Simulated electric field scattered by the RS metasurface. (e) Experiment setup and the fabricated metasurface prototype. (f) Simulated and experimentally measured far-field intensity pattern. The shaded area marks the measurement blind zone [-15 deg, 15 deg] due to the source antenna obstruction.

$|\Psi_{\mathrm{in}}\rangle \to |\Psi_{\mathrm{tra}}^+\rangle, |\Psi_{\mathrm{in}}\rangle \to |\Psi_{\mathrm{tra}}^-\rangle, |\Psi_{\mathrm{in}}\rangle \to |\Psi_{\mathrm{tra}}^+\rangle \to |\Psi_{\mathrm{ref}}^+\rangle$, and $|\Psi_{\mathrm{in}}\rangle \to |\Psi_{\mathrm{tra}}^-\rangle \to |\Psi_{\mathrm{ref}}^-\rangle$. As an example, Fig. 2e depicts the polarization evolutions associated with $|\Psi_{\mathrm{tra}}^+\rangle$ and $|\Psi_{\mathrm{ref}}^+\rangle$ for $\varepsilon = 1 + \mathrm{i}, \delta = 2, \phi = 30°$, and $\theta = 0°$. Notably, the electric and magnetic polarizations evolve along the same pathway on the E-sphere and H-sphere, which are independent of the RS polarization evolution on the RS-sphere. Figure 2f shows the total geometric phases (i.e., sum of PB and RS phases) induced by the four polarization evolutions for different $\alpha_{\mathrm{e}} = \frac{\phi}{2}$. The geometric phases (circles) agree with the transmission and reflection phases (solid lines) predicted by the Fresnel equations. Thus, the well-known reflection and transmission phases at interfaces can be interpreted as the geometric phases induced by 4D polarization evolution, uncovering the geometric origin of this fundamental optical phenomena.

RS phase at metasurfaces

The RS phase can also emerge at artificial interfaces such as electromagnetic metasurfaces, due to the modulation of local electric and magnetic responses. To demonstrate this, we propose an RS metasurface comprising metallic split rings with the same geometric dimensions, as shown in Fig. 3a. The metasurface is under the normal incidence of a plane wave with linearly polarized electric and magnetic fields. The corresponding incident RS field is $\mathbf{F}_1^{\mathrm{in}} = (\hat{\mathbf{e}}_x - \mathrm{i}\hat{\mathbf{h}}_y)Ee^{-\mathrm{i}k_0 z - \mathrm{i}\omega t}$; its polarization state can be labelled by the RS spin as $|\kappa_{\mathrm{in}} = -1\rangle$. The incident wave excites an electric dipole p_x and a magnetic dipole m_y in the meta-atoms, forming a RS dipole $\mathbf{D}_{\mathrm{rs}} = p_x\hat{\mathbf{e}}_x + \mathrm{i}m_y\hat{\mathbf{h}}_y$ and generating scattering fields in forward and backward directions. The scattering RS field is $\mathbf{F}_1^{\mathrm{out}} = (\hat{\mathbf{e}}_x + \mathrm{i}\kappa_{\mathrm{out}}\hat{\mathbf{h}}_y)Ee^{\mathrm{i}\kappa_{\mathrm{out}}k_0 z - \mathrm{i}\omega t}$ with polarization state $|\kappa_{\mathrm{out}} = \pm 1\rangle$. Denoting the polarization evolution as $|\kappa_{\mathrm{in}}\rangle \to |\kappa_{\mathrm{out}}\rangle$, the RS phase emerges in the cross-polarized channel $|-1\rangle \to |+1\rangle$ but vanishes in the co-polarized channel $|-1\rangle \to |-1\rangle$.

Figure 3b shows the RS polarization evolution in the channel $|-1\rangle \to |+1\rangle$. The incident state $|F_1^{\mathrm{in}}\rangle$ and backward scattering state $|F_1^{\mathrm{out}}\rangle$ are represented by the south and north poles, respectively. The polarization state of the RS dipole $\mathbf{D}_{\mathrm{rs}}$, denoted as $|D_{\mathrm{rs}}\rangle$, is located on the equator. The orientation angle of $\mathbf{D}_{\mathrm{rs}}$ in the constitutive frame is $\alpha_{\mathrm{rs}} = \arctan(\frac{\mathrm{i}m_y}{p_x})$. Rotating the meta-atoms around x or y direction will alter α_{rs} (Supplementary Note V) and change the azimuthal angle on the RS-sphere. The resulting RS phase is $\Phi_{\mathrm{rs}} = -2\alpha_{\mathrm{rs}}$. Notably, the PB phase
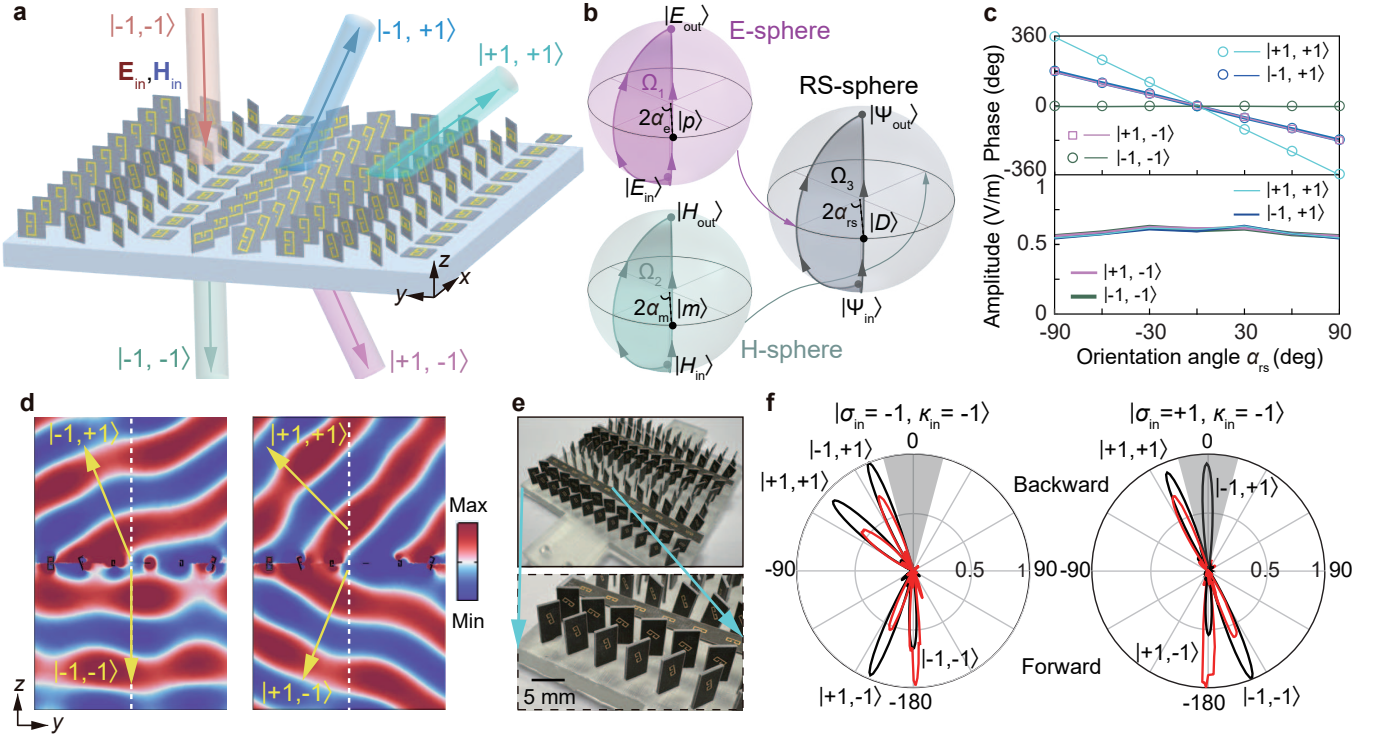
FIG. 4. **Complementary RS and PB phases at a metasurface**. (a) Schematic of the quadruplex RS meta-deflector under the normal incidence of a plane wave with LCP electric field. (b) 4D polarization evolution on the Poincaré hypersphere induced by the higher-order RS metasurface. (c) Theoretical geometric phase (symbols), simulated phase (solid lines), and simulated amplitude in four polarization evolution channels as a function of the orientation angle of RS dipole in the meta-atom. (d) Simulated electric field distribution of four output waves. (e) Fabricated metasurface prototype. (f) Simulated and experimentally measured far-field intensity pattern under orthogonal incidence. The shaded area marks the measurement blind zone [-15 deg, 15 deg] due to the source antenna obstruction.

vanishes in this case because the meta-atom rotation around x or y direction does not change the electric or magnetic polarization. Figure 3c shows the phases and amplitudes of the scattering fields as a function of the orientation angle α_{rs} of the RS dipole $\mathbf{D}_{rs}$. The simulated phases (solid lines) agree with the RS phase (circles) obtained by evaluating the solid angle in the RS-sphere. Notably, the phase of the backward scattering field $|+1\rangle$ exhibits a linear relationship with α_{rs}, while the phase of the forward scattering field $|-1\rangle$ is independent of α_{rs}. In addition, the scattering amplitudes remain approximately constant for different α_{rs}.

The RS metasurface in Fig. 3a can generate RS phase gradient along y direction, which can deflect the incident wave. Figure 3d shows the simulated electric field E_x scattered by the RS metasurface. We note that only the backward scattering field is deflected into oblique direction, and the wavefront is consistent with the deflection angle $\beta = \arcsin(\frac{1}{k_0}\frac{\Delta\Phi_{rs}}{\Delta y})$ predicted by the generalized Snell's law [59]. The deflection direction can be reversed by flipping the RS spin (i.e., propagation direction) of the incident plane wave (Supplementary Note VI). We conduct microwave experiments to verify the theory by using the experiment setup and metasurface in Fig. 3e (Methods). The measured far-field intensity scattered by the metasurface is shown as the red line in Fig. 3f, which agrees well with the simulation result denoted by the black line. Only the backward scattering lobe exhibits a deflection angle, confirming the validity of the theory.

To verify the high-dimensional geometric framework based on the RS and PB phases, we consider the higher-order RS metasurface in Fig. 4a under the incidence of a plane wave with circularly polarized electric and magnetic fields. Compared to the metasurface in Fig. 3a, the meta-atoms here are further rotated around the local z axis (Methods), which induces electric and magnetic polarization evolutions and gives rise to the additional PB phase Φ_{pb}. Consequently, the metasurface generates scattering fields carrying the total geometric phase $\Phi_{tot} = \Phi_{pb} + \Phi_{rs}$. The incident wave field is $\mathbf{\Psi}_{in} = [(\hat{\mathbf{e}}_x + i\sigma_{in}\hat{\mathbf{e}}_y) - i(\hat{\mathbf{h}}_y - i\sigma_{in}\hat{\mathbf{h}}_x)]Ee^{-ik_0z-i\omega t}$, which carries the spins $\sigma_{in} = -1$ and $\kappa_{in} = -1$. Its electric, magnetic, and RS polarization states are represented by the south poles on the E-sphere, H-sphere, and RS-sphere, respectively, as shown in Fig. 4b. The incident wave excites the 4D dipole in the meta-atoms: $\mathbf{D} = \mathbf{p} + i\mathbf{m} = [(p_x\hat{\mathbf{e}}_x + p_y\hat{\mathbf{e}}_y) + i(m_y\hat{\mathbf{h}}_y + m_x\hat{\mathbf{h}}_x)]e^{-i\omega t}$. The polarization states of the electric, magnetic,
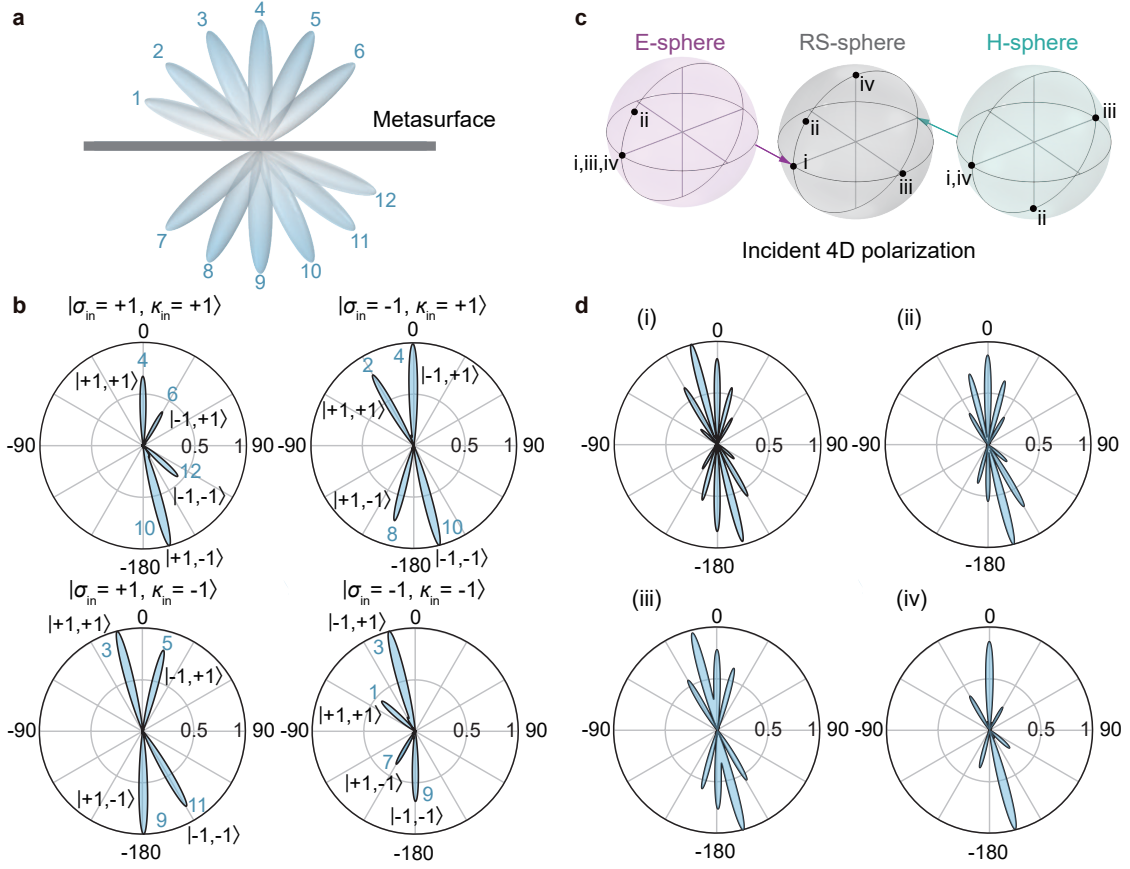
FIG. 5. **Reconfigurable wave deflection by the general RS metasurface**. (a) Schematic of the multiplexed beam forming with twelve distinct output wavefronts. (b) Simulated far-field intensity patterns under the normal incidence of plane waves with orthogonal 4D polarizations. The lobes are labelled in accordance with (a). (c) Incident 4D polarizations (labelled as "i-iv") for achieving reconfigurable far-field intensity patterns. (d) Far-field intensity patterns with different number of lobes induced by the incident polarizations "i-iv" in (c).

and RS dipoles are represented by $|p\rangle, |m\rangle$, and $|D_{\text{rs}}\rangle$ on the equators with the azimuthal angles $2\alpha_{\text{p}}, 2\alpha_{\text{m}}$, and $2\alpha_{\text{rs}}$, respectively. Here, $\alpha_{\text{p}} (\alpha_{\text{m}})$ is the orientation angle of the electric (magnetic) dipole in the coordinate frame; α_{rs} is the orientation angle of the RS dipole in the constitutive frame. The meta-atoms in Fig. 4a are designed to satisfy $\alpha_{\text{p}} = \alpha_{\text{rs}}$. The metasurface generates the scattering field $\mathbf{\Psi}_{\text{out}} = [(\hat{\mathbf{e}}_x + i\sigma_{\text{out}}\hat{\mathbf{e}}_y) + i\kappa_{\text{out}}(\hat{\mathbf{h}}_y - i\sigma_{\text{out}}\hat{\mathbf{h}}_x)]Ee^{i\kappa_{\text{out}}k_0z - i\omega t}$, which has four polarization components $|\sigma_{\text{out}} = \pm1, \kappa_{\text{out}} = \pm1\rangle$, as shown in Fig. 4a. Correspondingly, there are four polarization evolution channels $|\sigma_{\text{in}}, \kappa_{\text{in}}\rangle \rightarrow |\sigma_{\text{out}}, \kappa_{\text{out}}\rangle$. Figure 4b shows the 4D polarization evolution in the channel $|-1, -1\rangle \rightarrow |+1, +1\rangle$ as an example. The resulting geometric phase is:

$$\Phi_{\text{tot}} = \Phi_{\text{pb}} + \Phi_{\text{rs}} = (\sigma_{\text{in}} - \sigma_{\text{out}})\alpha_{\text{p}} + (\kappa_{\text{in}} - \kappa_{\text{out}})\alpha_{\text{rs}}. \tag{1}$$

Figure 4c shows the phases and amplitudes of the four output waves for different orientation angle α_{rs}. The simulated phases (solid lines) are consistent with the total geometric phases (symbols) given by the solid angles on the Poincaré hypersphere, confirming the emergence of both the PB and RS phases. The simulated amplitudes of different outputs are approximately equal and nearly independent of α_{rs}.

Figure 4d shows the simulated electric fields of the four output waves. The wavefronts are consistent with the deflection directions (yellow arrows) predicted based on the geometric phase gradient. Specifically, the output $|+1, +1\rangle$ exhibits the largest deflection angle; $|+1, -1\rangle$ and $|-1, +1\rangle$ exhibit the same deflection angle; $|-1, -1\rangle$ undergoes no deflection. The number of distinct output wavefronts can be increased by flipping the electric spin and RS spin of the incident wave (Supplementary Notes VII and VIII). Figure 4e shows the fabricated metasurface sample comprising two supercells. The scattering far-field intensities under the incidence of the plane waves $|\sigma_{\text{in}} = \pm1, \kappa_{\text{in}} = -1\rangle$ are shown in Fig. 4f. We notice that a total of eight output intensity lobes (four lobes in each case) emerge in six distinct directions, with consistency between the experimental (red lines) and simulation (black lines) results. Unlike the case in Fig. 4c, the intensities of different outputs are not equal due to the finite size of the metasurface.

The output wavefronts can be further increased in the higher-order RS metasurface with $\alpha_p = \alpha_m \neq \alpha_{rs}$. Under the incidence of the plane waves $|\sigma_{in} = \pm 1, \kappa_{in} = \pm 1\rangle$, this metasurface can generate twelve output wavefronts propagating in different directions, as schematically shown in Fig. 5a. The simulated far-field intensity patterns are shown in Fig. 5b, where the intensity lobes are labelled in accordance with the numbers in Fig. 5a. As seen, the scattered far fields can propagate in twelve different directions, depending on the values of σ_{out} and κ_{out}. Additionally, the number of distinct outputs can be dynamically reconfigured by employing the incident wave $|\Psi_{in}\rangle = \eta_1| + 1, +1\rangle + \eta_2| + 1, -1\rangle + \eta_3| - 1, +1\rangle + \eta_4| - 1, -1\rangle$ with varying 4D polarization. For example, by tuning the coefficients η_{1-4} to obtain four different incident polarizations, denoted by the points "i-iv" on the Poincaré hypersphere in Fig. 5c, the metasurface can generate 12, 10, 8, and 6 far-field intensity lobes, as shown in Fig. 5d. These results demonstrate the practical application potential of the framework, which can be further enriched by introducing time-varying or active components into the system [60–63].

Discussion

We unveil the geometric phases arising from complete electromagnetic polarization evolution in the 4D RS space by treating electromagnetic waves as a four-component bispinor. Beyond the conventional PB phase induced by electric or magnetic polarization evolution, we discover a new geometric phase, the RS phase, which originates from the hybrid electric-magnetic polarization evolution and can manifest even in linearly polarized waves. The complementary RS and PB phases enable a unified high-dimensional geometric framework for understanding and controlling phase shifts in light propagation across general interfaces, including artificial metasurfaces. The proposed mechanism applies to general electromagnetic waves, including evanescent waves and complex structured waves. Our work broadens the geometric phase paradigm and offers fundamental insights into the geometric nature of light-matter interactions, opening new avenues for exploring topological and non-Abelian phenomena in high-dimensional classical wave systems. Future research may integrate the spin-redirection geometric phase [10, 11] arising from variations of propagation direction into this framework, which promises a more comprehensive approach for geometric phase physics.

After the initial posting of this work [64], a related preprint appeared [65], proposing an "electric-magnetic (EM) geometric phase" arising from cyclic evolution of the **E**–**H** relationship in nonparaxial light. This EM geometric phase is conceptually equivalent to the RS geometric phase described here and can be regarded as a special case within our broader high-dimensional framework based on the 4D RS space. The RS geometric phase applies to general electromagnetic waves, including nonparaxial waves (e.g., evanescent waves and structured waves). Their conclusion that EM geometric phase appears exclusively in nonparaxial light does not conflict with our results, as their analysis does not address the scenarios involving material interfaces, where the local **E**–**H** relationship can be modified. We view their work as complementary to ours, together contributing to a more complete understanding of this geometric phase across different wave regimes.

Methods

Poincaré hypersphere representation

The 4D electromagnetic polarization can be represented on the Poincaré hypersphere in Fig. 1a. The north and south poles of the E-sphere are $|N_e\rangle = \frac{1}{\sqrt{2}} (\hat{\mathbf{e}}_i + i\hat{\mathbf{e}}_j)$ and $|S_e\rangle = \frac{1}{\sqrt{2}} (\hat{\mathbf{e}}_i - i\hat{\mathbf{e}}_j)$, respectively. The north and south poles of the H-sphere are $|N_m\rangle = \frac{1}{\sqrt{2}}(\hat{\mathbf{h}}_j - i\hat{\mathbf{h}}_i)$ and $|S_m\rangle = \frac{1}{\sqrt{2}}(\hat{\mathbf{h}}_j + i\hat{\mathbf{h}}_i)$, respectively. Any 4D polarization state $|\Psi\rangle$ can be parameterized by six parameters $(\theta_e, \phi_e, \theta_m, \phi_m, \theta_{rs}, \phi_{rs})$ as

$$
\begin{aligned}
|\Psi\rangle = &\frac{1}{\sqrt{2}} \left[\cos\left(\frac{\theta_{rs}}{2}\right) e^{-i\frac{\phi_{rs}}{2}} + \sin\left(\frac{\theta_{rs}}{2}\right) e^{i\frac{\phi_{rs}}{2}} \right] |H_{rs}\rangle \\
&+ i\frac{1}{\sqrt{2}} \left[\cos\left(\frac{\theta_{rs}}{2}\right) e^{-i\frac{\phi_{rs}}{2}} - \sin\left(\frac{\theta_{rs}}{2}\right) e^{i\frac{\phi_{rs}}{2}} \right] |V_{rs}\rangle ,
\end{aligned}
\tag{2}
$$

where $|H_{rs}\rangle = \cos\left(\frac{\theta_e}{2}\right) e^{-\frac{i\phi_e}{2}} |N_e\rangle + \sin\left(\frac{\theta_e}{2}\right) e^{\frac{i\phi_e}{2}} |S_e\rangle$ represents an arbitrary state on the E-sphere and $|V_{rs}\rangle = \cos\left(\frac{\theta_m}{2}\right) e^{-\frac{i\phi_m}{2}} |N_m\rangle + \sin\left(\frac{\theta_m}{2}\right) e^{\frac{i\phi_m}{2}} |S_m\rangle$ represents an arbitrary state on the H-sphere. The representation of the electric (magnetic) polarization on the E-sphere (H-sphere) has been well established in the literature. The representation of the hybrid **E-H** polarization on the RS-sphere can be understood by considering the RS vector $\mathbf{F}_1 = E_i\hat{\mathbf{e}}_i + iH_j\hat{\mathbf{h}}_j$ of paraxial waves as an example ($\mathbf{F}_2$ exhibits the same polarization and can be represented similarly). The temporal evolution of $\mathbf{F}_1$ traces out a polarization ellipse on the plane with the bases $(\hat{\mathbf{e}}_i, \hat{\mathbf{h}}_j)$, where the polarization ellipticity and orientation are determined by the relative magnitude and phase of E_i and H_j. The polarization of $\mathbf{F}_1$ can be mapped to a point on the RS-sphere with the normalized RS Stokes vector (S_1, S_2, S_3),

where $S_1 = \frac{|E_i|^2 - |H_j|^2}{|E_i|^2 + |H_j|^2}$, $S_2 = \frac{2\,\mathrm{Re}[E_i(iH_j)^*]}{|E_i|^2 + |H_j|^2} = \frac{2\,\mathrm{Im}[E_i H_j^*]}{|E_i|^2 + |H_j|^2}$, and $S_3 = \frac{-2\,\mathrm{Im}[E_i(iH_j)^*]}{|E_i|^2 + |H_j|^2} = \frac{2\,\mathrm{Re}[E_i H_j^*]}{|E_i|^2 + |H_j|^2}$. Importantly, S_1 is determined by the relative amplitude of E_i and H_j; S_2 and S_3 are determined by the imaginary and real parts of the complex Poynting vector, respectively.

Some representative RS polarization states and corresponding E_i-H_j relations are shown in Fig. S1. The points located at $\phi = 0$ longitudinal line correspond to propagating waves in transparent media with a real Poynting vector. Specifically, the north and south poles denote the free-space propagating waves in opposite directions. The points on the equator represent purely evanescent waves with an imaginary Poynting vector, e.g., waves in lossless electric/magnetic plasma media. The remaining points on the sphere denote waves in lossy or gain media with a complex Poynting vector.

Numerical simulation

All the full-wave numerical simulations are performed with the package COMSOL Multiphysics. In the simulation of the metasurfaces in Figs. 3-5, we set the periods of unit cells along x and y directions to be $L_x = L_y = 5.5$ mm. The working frequency is 24 GHz. In each unit cell, the split ring has two arms with geometric parameters: $t_1 = 0.035$ mm, $t_2 = 0.15$ mm, $h = 1$ mm, $w = 2.3$ mm, $l = 0.58$ mm, and $g = 0.27$ mm (refer to Fig. 3a for the definition of the geometric parameters). The split rings are made of copper with the electrical conductivity $\sigma = 5.814 \times 10^7$ S/m. To change the 4D dipole polarization of the meta-atom, we rotate the split ring around the x, y, and z axis by angles α_x, α_y, and α_z, respectively. For the numerical demonstration in Fig. 3, each supercell comprises six split rings with the rotation angles $(\alpha_x, \alpha_y, \alpha_z)$ in degrees: $(0, -90, 0)$, $(0, -68, 0)$, $(0, 0, 0)$, $(-90, 0, 0)$, $(0, 180, 0)$, and $(0, 112, 0)$. For the numerical demonstration in Fig. 4, each supercell comprises six split rings with the rotation angles $(\alpha_x, \alpha_y, \alpha_z)$ in degrees: $(0, -90, -90)$, $(0, -68, -60)$, $(0, 0, -30)$, $(-90, 0, 0)$, $(0, 180, 30)$, and $(0, 112, 60)$. For the numerical demonstration in Fig. 5, each supercell comprises six split rings with the rotation angles $(\alpha_x, \alpha_y, \alpha_z)$ in degrees: $(0, 82, -160)$, $(0, 68, -120)$, $(0, 45, -80)$, $(-45, 0, -40)$, $(-90, 0, 0)$, $(-130, 0, 40)$, $(0, 135, 80)$, $(0, 112, 120)$, and $(0, 96, 160)$. To obtain the incident 4D polarizations "i-iv" in Fig. 5c, we set the coefficients $(\eta_1, \eta_2, \eta_3, \eta_4) = (\frac{1}{2}, \frac{1}{2}, \frac{1}{2}, \frac{1}{2})$ for "i", $(\frac{1}{\sqrt{3}}, \frac{1}{\sqrt{3}}, \frac{1}{\sqrt{3}}, 0)$ for "ii", $(0, \frac{1}{\sqrt{2}}, \frac{1}{\sqrt{2}}, 0)$ for "iii", and $(\frac{1}{\sqrt{2}}, 0, \frac{1}{\sqrt{2}}, 0)$ for "iv".

Experiment

The metasurfaces are fabricated on a Roger's 5880 substrate with printed circuit board technology (thickness $t_s = 0.508$ mm, height $h_s = 4$ mm, relative permittivity $\varepsilon_r = 2.2$, and loss tangent $\tan \delta = 0.0009$). Experimental characterization is performed in a microwave anechoic chamber to suppress multi-path effects. The setup comprises a linearly polarized transmitting horn antenna, a receiving horn antenna (Rx), and a vector network analyzer (VNA, Keysight PNA 5227B). Both antennas are positioned 1 m from the metasurface and connected to the two ports of the VNA via 50Ω coaxial cables. By rotating the angular position of the Rx horn antenna with respect to the metasurface and measuring the transmitted/reflected signals by the VNA, the far-field scattering pattern of the metasurface is obtained. For the measurements in Fig. 4, wideband 3D-printed polarizers are mounted on the horn apertures to generate and detect circularly polarized waves. Prior to characterizing the metasurface, a background signal measurement is performed without the sample to capture the direct coupling between the source and receiver as well as other ambient contributions. The measured background signals are then used for calibration to minimize the contributions of these spurious signals to the measurement.

Acknowledgements

Author Contributions

S.W. and Y.C. conceived the idea and developed the concepts. Y.C. designed the structures and conducted the numerical simulations. Y.-S.Z., Y.C., and G.-B.W. designed and carried out the experiments. Y.C. and S.W. wrote the draft. S.W., G.-B.W., and D.P.T. supervised the project. All authors contributed to discussions, interpretation of the results, and polishing of the manuscript.

References

1. Pancharatnam, S. Generalized theory of interference, and its applications. *Proc. Indian Acad. Sci. Sect. A* **44**, 247–262 (1956).
2. Berry, M. V. Quantal phase factors accompanying adiabatic changes. *Proc. R. Soc. Lond. A* **392**, 45–57 (1984).
3. Shapere, A. & Wilczek, F. *Geometric phases in physics* (World scientific, 1989).
4. Cohen, E., Larocque, H., Bouchard, F., Nejadsattari, F., Gefen, Y. & Karimi, E. Geometric phase from Aharonov–Bohm to Pancharatnam–Berry and beyond. *Nat. Rev. Phys.* **1**, 437–449 (2019).
5. Simon, B. Holonomy, the quantum adiabatic theorem, and Berry's phase. *Phys. Rev. Lett.* **51**, 2167–2170 (1983).
6. Aharonov, Y. & Anandan, J. Phase change during a cyclic quantum evolution. *Phys. Rev. Lett.* **58**, 1593–1596 (1987).
7. Mead, C. A. The geometric phase in molecular systems. *Rev. Mod. Phys.* **64**, 51–85 (1992).
8. Xiao, D., Chang, M.-C. & Niu, Q. Berry phase effects on electronic properties. *Rev. Mod. Phys.* **82**, 1959–2007 (2010).
9. Liu, T., Qiang, X.-B., Lu, H.-Z. & Xie, X. Quantum geometry in condensed matter. *Natl. Sci. Rev.* **12**, nwae334 (2025).
10. Tomita, A. & Chiao, R. Y. Observation of Berry's topological phase by use of an optical fiber. *Phys. Rev. Lett.* **57**, 937–940 (1986).
11. Chiao, R. Y. & Wu, Y.-S. Manifestations of Berry's topological phase for the photon. *Phys. Rev. Lett.* **57**, 933 (1986).
12. Bliokh, K. Y., Gorodetski, Y., Kleiner, V. & Hasman, E. Coriolis effect in optics: unified geometric phase and spin-Hall effect. *Phys. Rev. Lett.* **101**, 030404 (2008).
13. Wang, S., Ma, G. & Chan, C. T. Topological transport of sound mediated by spin-redirection geometric phase. *Sci. Adv.* **4**, eaaq1475 (2018).
14. Wang, J., Valligatla, S., Yin, Y., Schwarz, L., Medina-Sánchez, M., Baunack, S., Lee, C. H., Thomale, R., Li, S. & Fomin, V. M. Experimental observation of Berry phases in optical Möbius-strip microcavities. *Nat. Photonics* **17**, 120–125 (2023).
15. Bliokh, K. Y., Rodríguez-Fortuño, F. J., Nori, F. & Zayats, A. V. Spin–orbit interactions of light. *Nat. Photonics* **9**, 796–808 (2015).
16. Haldane, F. D. M. & Raghu, S. Possible realization of directional optical waveguides in photonic crystals with broken time-reversal symmetry. *Phys. Rev. Lett.* **100**, 013904 (2008).
17. Wang, Z., Chong, Y., Joannopoulos, J. D. & Soljačić, M. Observation of unidirectional backscattering-immune topological electromagnetic states. *Nature* **461**, 772–775 (2009).
18. Lu, L., Joannopoulos, J. D. & Soljačić, M. Topological photonics. *Nat. Photonics* **8**, 821–829 (2014).
19. Ozawa, T., Price, H. M., Amo, A., Goldman, N., Hafezi, M., Lu, L., Rechtsman, M. C., Schuster, D., Simon, J. & Zilberberg, O. Topological photonics. *Rev. Mod. Phys.* **91**, 015006 (2019).
20. Bliokh, K. Y., Alonso, M. A. & Dennis, M. R. Geometric phases in 2D and 3D polarized fields: geometrical, dynamical, and topological aspects. *Rep. Prog. Phys.* **82**, 122401 (2019).
21. Cisowski, C., Götte, J. & Franke-Arnold, S. Colloquium: Geometric phases of light: Insights from fiber bundle theory. *Rev. Mod. Phys.* **94**, 031001 (2022).
22. Fu, T., Zhang, R.-Y., Jia, S., Chan, C. & Wang, S. Near-field spin Chern number quantized by real-space topology of optical structures. *Phys. Rev. Lett.* **132**, 233801 (2024).
23. Bomzon, Z., Biener, G., Kleiner, V. & Hasman, E. Space-variant Pancharatnam–Berry phase optical elements with computer-generated subwavelength gratings. *Opt. Lett.* **27**, 1141–1143 (2002).
24. Yin, X., Ye, Z., Rho, J., Wang, Y. & Zhang, X. Photonic spin Hall effect at metasurfaces. *Science* **339**, 1405–1407 (2013).
25. Wang, S., Wu, P. C., Su, V.-C., Lai, Y.-C., Chen, M.-K., Kuo, H. Y., Chen, B. H., Chen, Y. H., Huang, T.-T., Wang, J.-H., Lin, R.-M., Kuan, C.-H., Li, T., Wang, Z., Zhu, S. & Tsai, D. P. A broadband achromatic metalens in the visible. *Nat. Nanotechnol.* **13**, 227–232 (2018).
26. Peng, J., Zhang, R.-Y., Jia, S., Liu, W. & Wang, S. Topological near fields generated by topological structures. *Sci. Adv.* **8**, eabq0910 (2022).
27. Kim, G., Kim, Y., Yun, J., Moon, S.-W., Kim, S., Kim, J., Park, J., Badloe, T., Kim, I. & Rho, J. Metasurface-driven full-space structured light for three-dimensional imaging. *Nat. Commun.* **13**, 5920 (2022).
28. Xiong, B., Liu, Y., Xu, Y., Deng, L., Chen, C.-W., Wang, J.-N., Peng, R., Lai, Y., Liu, Y. & Wang, M. Breaking the limitation of polarization multiplexing in optical metasurfaces with engineered noise. *Science* **379**, 294–299 (2023).
29. Lin, D., Fan, P., Hasman, E. & Brongersma, M. L. Dielectric gradient metasurface optical elements. *Science* **345**, 298–302 (2014).
30. Tymchenko, M., Gomez-Diaz, J. S., Lee, J., Nookala, N., Belkin, M. A. & Alù, A. Gradient nonlinear Pancharatnam-Berry metasurfaces. *Phys. Rev. Lett.* **115**, 207403 (2015).
31. Devlin, R. C., Ambrosio, A., Rubin, N. A., Mueller, J. B. & Capasso, F. Arbitrary spin-to–orbital angular momentum conversion of light. *Science* **358**, 896–901 (2017).
32. Yuan, Y., Zhang, K., Ratni, B., Song, Q., Ding, X., Wu, Q., Burokur, S. N. & Genevet, P. Independent phase modulation for quadruplex polarization channels enabled by chirality-assisted geometric-phase metasurfaces. *Nat. Commun.* **11**, 4186 (2020).
33. Wang, B., Liu, W., Zhao, M., Wang, J., Zhang, Y., Chen, A., Guan, F., Liu, X., Shi, L. & Zi, J. Generating optical vortex beams by momentum-space polarization vortices centred at bound states in the continuum. *Nat. Photonics* **14**, 623–628 (2020).
34. Song, Q., Odeh, M., Zúñiga-Pérez, J., Kanté, B. & Genevet, P. Plasmonic topological metasurface by encircling an exceptional point. *Science* **373**, 1133–1137 (2021).

35. Xiao, W. & Wang, S. On-chip optical wavefront shaping by transverse-spin-induced Pancharatanam–Berry phase. *Opt. Lett.* **49**, 1915–1918 (2024).

36. Pan, H., Chen, M. K., Tsai, D. P. & Wang, S. Nonreciprocal Pancharatnam-Berry metasurface for unidirectional wavefront manipulations. *Opt. Express* **32**, 25632–25643 (2024).

37. Zeng, Y., Sha, X., Zhang, C., Zhang, Y., Deng, H., Lu, H., Qu, G., Xiao, S., Yu, S., Kivshar, Y. et al. Metalasers with arbitrarily shaped wavefront. *Nature* **643**, 1240–1245 (2025).

38. Berry, M. V. The adiabatic phase and Pancharatnam's phase for polarized light. *J. Mod. Opt.* **34**, 1401–1407 (1987).

39. Bhandari, R. & Samuel, J. Observation of topological phase by use of a laser interferometer. *Phys. Rev. Lett.* **60**, 1211–1213 (1988).

40. Barnett, S. M. Optical Dirac equation. *New J. Phys.* **16**, 093008 (2014).

41. Alpeggiani, F., Bliokh, K., Nori, F. & Kuipers, L. Electromagnetic helicity in complex media. *Phys. Rev. Lett.* **120**, 243605 (2018).

42. Nye, J. F. & Hajnal, J. The wave structure of monochromatic electromagnetic radiation. *Proc. R. Soc. Lond. A* **409**, 21–36 (1987).

43. Bialynicki-Birula, I. V photon wave function. *Prog. Opt.* **36**, 245–294 (1996).

44. Kemp, C. J., Cooper, N. R. & Ünal, F. N. Nested-sphere description of the N-level Chern number and the generalized Bloch hypersphere. *Phys. Rev. Res.* **4**, 023120 (2022).

45. Zhang, Z., Zhao, H., Wu, S., Wu, T., Qiao, X., Gao, Z., Agarwal, R., Longhi, S., Litchinitser, N. M. & Ge, L. Spin–orbit microlaser emitting in a four-dimensional Hilbert space. *Nature* **612**, 246–251 (2022).

46. Weber, H. *Die partiellen Differential-Gleichungen der mathematischen Physik nach Riemann's Vorlesungen* (F. Vieweg & sohn, 1901).

47. Silberstein, L. Elektromagnetische grundgleichungen in bivektorieller behandlung. *Ann. Phys. (Berlin)* **327**, 579–586 (1907).

48. Silberstein, L. Nachtrag zur abhandlung über „elektromagnetische grundgleichungen in bivektorieller behandlung". *Ann. Phys. (Berlin)* **329**, 783–784 (1907).

49. Bialynicki-Birula, I. Photon wave function. *Prog. Opt.* **36**, 245–294 (1996).

50. Bialynicki-Birula, I. & Bialynicka-Birula, Z. The role of the riemann–silberstein vector in classical and quantum theories of electromagnetism. *J. Phys. A: Math. Theor.* **46**, 053001 (2013).

51. Bliokh, K. Y., Bekshaev, A. Y. & Nori, F. Dual electromagnetism: helicity, spin, momentum and angular momentum. *New J. Phys.* **15**, 033026 (2013).

52. Neugebauer, M., Eismann, J. S., Bauer, T. & Banzer, P. Magnetic and electric transverse spin density of spatially confined light. *Phys. Rev. X* **8**, 021042 (2018).

53. Wang, S., Hou, B., Lu, W., Chen, Y., Zhang, Z. & Chan, C. T. Arbitrary order exceptional point induced by photonic spin–orbit interaction in coupled resonators. *Nat. Commun.* **10**, 832 (2019).

54. Shi, P., Du, L., Li, C., Zayats, A. V. & Yuan, X. Transverse spin dynamics in structured electromagnetic guided waves. *Proc. Natl. Acad. Sci. U.S.A.* **118**, e2018816118 (2021).

55. Eismann, J., Nicholls, L., Roth, D., Alonso, M. A., Banzer, P., Rodríguez-Fortuño, F., Zayats, A., Nori, F. & Bliokh, K. Transverse spinning of unpolarized light. *Nat. Photonics* **15**, 156–161 (2021).

56. Vernon, A. J., Golat, S., Rigouzzo, C., Lim, E. A. & Rodriguez-Fortuno, F. J. A decomposition of light's spin angular momentum density. *Light Sci. Appl.* **13**, 160 (2024).

57. Golat, S., Vernon, A. J. & Rodríguez-Fortuño, F. J. The electromagnetic symmetry sphere: a framework for energy, momentum, spin and other electromagnetic quantities. *Phys. Scripta* **100**, 105518 (2025).

58. Jackson, J. D. *Classical electrodynamics* (John Wiley & Sons, 1999).

59. Yu, N., Genevet, P., Kats, M. A., Aieta, F., Tetienne, J.-P., Capasso, F. & Gaburro, Z. Light propagation with phase discontinuities: generalized laws of reflection and refraction. *Science* **334**, 333–337 (2011).

60. Zhang, L., Chen, X. Q., Liu, S., Zhang, Q., Zhao, J., Dai, J. Y., Bai, G. D., Wan, X., Cheng, Q., Castaldi, G., Galdi, V. & Cui, T. J. Space-time-coding digital metasurfaces. *Nat. Commun.* **9**, 4334 (2018).

61. Shaltout, A. M., Shalaev, V. M. & Brongersma, M. L. Spatiotemporal light control with active metasurfaces. *Science* **364**, eaat3100 (2019).

62. Galiffi, E., Tirole, R., Yin, S., Li, H., Vezzoli, S., Huidobro, P. A., Silveirinha, M. G., Sapienza, R., Alù, A. & Pendry, J. B. Photonics of time-varying media. *Adv. Photonics* **4**, 014002 (2022).

63. Tirole, R., Vezzoli, S., Galiffi, E., Robertson, I., Maurice, D., Tilmann, B., Maier, S. A., Pendry, J. B. & Sapienza, R. Double-slit time diffraction at optical frequencies. *Nat. Phys.* **19**, 999–1002 (2023).

64. Cheng, Y., Zeng, Y.-S., Xiao, W., Fu, T., Wu, J., Wu, G.-B., Tsai, D. P. & Wang, S. Riemann-Silberstein geometric phase for high-dimensional light manipulation. *Preprint at https://arxiv.org/abs/2510.09112* (2025).

65. Vernon, A. J. & Bliokh, K. Y. Electric-magnetic geometric phase. *Preprint at https://arxiv.org/abs/2511.10348* (2025).

Supplementary Information for

Riemann-Silberstein geometric phase in 4D polarization space

Yuqiong Cheng,[1,*] Yuan-Song Zeng,[2,3,*] Wanyue Xiao,[1] Tong Fu,[1] Jiajun Wu,[2]

Geng-Bo Wu,[2,3,†] Din Ping Tsai,[1,2,3,‡] and Shubo Wang[1,§]

[1]Department of Physics, City University of Hong Kong, Kowloon, Hong Kong, China

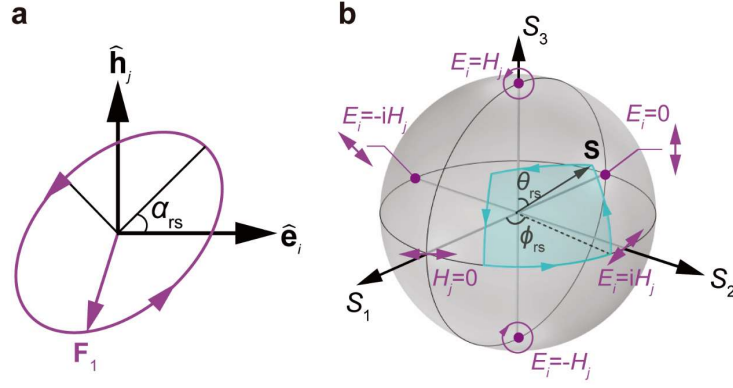*[2]Department of Electrical Engineering, City University of Hong Kong, Kowloon, Hong Kong, China*

[3]State Key Laboratory of Terahertz and Millimeter Waves, City University of Hong Kong, Kowloon, Hong Kong, China

Supplementary Figures S1-S9

Supplementary Notes

Fig. S1 (a) RS polarization ellipse. (b) Representation of RS polarization on the RS-sphere.

I. Effective Hamiltonian of 4D polarization state

Using the basis $\{\ |N_e\rangle, |S_e\rangle, |N_m\rangle, |S_m\rangle\ \}$, the 4D polarization state can be expressed as $|\psi\rangle = \left[A\cos\left(\frac{\theta_e}{2}\right)e^{-\frac{i\phi_e}{2}}, A\sin\left(\frac{\theta_e}{2}\right)e^{\frac{i\phi_e}{2}}, B\cos\left(\frac{\theta_m}{2}\right)e^{-\frac{i\phi_m}{2}}, B\sin\left(\frac{\theta_m}{2}\right)e^{\frac{i\phi_m}{2}}\right]^{\mathrm{T}}$, where $A = \frac{1}{\sqrt{2}}\left[\cos\left(\frac{\theta_{rs}}{2}\right)e^{-\frac{i\phi_{rs}}{2}} + \sin\left(\frac{\theta_{rs}}{2}\right)e^{\frac{i\phi_{rs}}{2}}\right]$ and $B = \frac{i}{\sqrt{2}}\left[\cos\left(\frac{\theta_{rs}}{2}\right)e^{-\frac{i\phi_{rs}}{2}} - \sin\left(\frac{\theta_{rs}}{2}\right)e^{\frac{i\phi_{rs}}{2}}\right]$. The effective Hamiltonian of the 4D polarization state is given by

$$\widehat{H} = |\psi\rangle\langle\psi| - \frac{1}{4}\hat{I}_4 = \begin{bmatrix} M_1 & M_2 \\ M_3 & M_4 \end{bmatrix} \tag{S1}$$

with

$$M_1 = \begin{bmatrix} |A|^2\cos^2\left(\frac{\theta_e}{2}\right) - \frac{1}{4} & \frac{1}{2}|A|^2\sin\theta_e\, e^{-i\phi_e} \\ \frac{1}{2}|A|^2\sin\theta_e\, e^{i\phi_e} & |A|^2\sin^2\left(\frac{\theta_e}{2}\right) - \frac{1}{4} \end{bmatrix}, \tag{S2}$$

$$M_2 = M_3^\dagger = \begin{bmatrix} AB^*\cos\left(\frac{\theta_e}{2}\right)\cos\left(\frac{\theta_m}{2}\right)e^{\frac{i(\phi_m-\phi_e)}{2}} & AB^*\cos\left(\frac{\theta_e}{2}\right)\sin\left(\frac{\theta_m}{2}\right)e^{\frac{-i(\phi_m+\phi_e)}{2}} \\ AB^*\sin\left(\frac{\theta_e}{2}\right)\cos\left(\frac{\theta_m}{2}\right)e^{\frac{i(\phi_m+\phi_e)}{2}} & AB^*\sin\left(\frac{\theta_e}{2}\right)\sin\left(\frac{\theta_m}{2}\right)e^{\frac{i(\phi_e-\phi_m)}{2}} \end{bmatrix}, \tag{S3}$$

$$M_4 = \begin{bmatrix} |B|^2\cos^2\left(\frac{\theta_m}{2}\right) - \frac{1}{4} & \frac{1}{2}|B|^2\sin\theta_m\, e^{-i\phi_m} \\ \frac{1}{2}|B|^2\sin\theta_m\, e^{i\phi_m} & |B|^2\sin^2\left(\frac{\theta_m}{2}\right) - \frac{1}{4} \end{bmatrix}. \tag{S4}$$

This Hamiltonian can be expanded using the basis of the generalized Gell-Mann matrices $\{\hat{\lambda}_1, \hat{\lambda}_2, \dots, \hat{\lambda}_{15}\}$:

$$\widehat{H} = \frac{1}{2}\mathbf{S}\cdot\hat{\boldsymbol{\lambda}} = \frac{1}{2}|A|^2\mathbf{S}_e\cdot\hat{\boldsymbol{\lambda}}_e + \frac{1}{2}|B|^2\mathbf{S}_m\cdot\hat{\boldsymbol{\lambda}}_m + \frac{1}{2}\mathbf{S}_{rs}\cdot(U^\dagger\hat{\boldsymbol{\lambda}}_{rs}U), \tag{S5}$$

where $\mathbf{S}_e = (\sin\theta_e\cos\phi_e, \sin\theta_e\sin\phi_e, \cos\theta_e)$, $\mathbf{S}_m = (\sin\theta_m\cos\phi_m, \sin\theta_m\sin\phi_m, \cos\theta_m)$, and $\mathbf{S}_{rs} = (\sin\theta_{rs}\cos\phi_{rs}, \sin\theta_{rs}\sin\phi_{rs}, \cos\theta_{rs})$ are three Stokes vectors; $\hat{\boldsymbol{\lambda}}_e = \{\hat{\lambda}_1, \hat{\lambda}_2, \hat{\lambda}_3\}$, $\hat{\boldsymbol{\lambda}}_m = \{\hat{\lambda}_{13}, \hat{\lambda}_{14}, \frac{1}{3}(\sqrt{6}\hat{\lambda}_{15} - \sqrt{3}\hat{\lambda}_8)\}$, and $\hat{\boldsymbol{\lambda}}_{rs} = \{\frac{1}{6}(2\sqrt{3}\hat{\lambda}_8 + \sqrt{6}\hat{\lambda}_{15}), \hat{\lambda}_4, \hat{\lambda}_5\}$ are vectors of the generalized Gell-Mann matrices; $U = e^{\frac{i\phi_e}{2}}e^{i\frac{\theta_e}{2}\mathbf{n}_e\cdot\hat{\boldsymbol{\sigma}}} \oplus e^{\frac{i\phi_m}{2}}e^{i\frac{\theta_m}{2}\mathbf{n}_m\cdot\hat{\boldsymbol{\sigma}}}$ implements unitary transformation of the bispinor polarization state with $\mathbf{n}_e = (-\sin\phi_e, \cos\phi_e, 0)$ and $\mathbf{n}_m = (-\sin\phi_m, \cos\phi_m, 0)$. In the above equation, the first term (i.e., $\frac{1}{2}|A|^2\mathbf{S}_e\cdot\hat{\boldsymbol{\lambda}}_e$) governs the electric polarization state in the interior electric space, which

can be represented on the E-sphere. The second term (i.e., $\frac{1}{2}|B|^2 \mathbf{S}_m \cdot \hat{\boldsymbol{\lambda}}_m$) governs the magnetic polarization state in the interior magnetic space, which can be represented on the H-sphere. The third term (i.e., $\frac{1}{2}\mathbf{S}_{rs} \cdot (U^\dagger\hat{\boldsymbol{\lambda}}_{rs}U)$) governs the hybrid electric-magnetic polarization, i.e., the mixing of the E-sphere and H-sphere in the exterior space, which can be represented on the RS-sphere. The three Stokes vectors $\mathbf{S}_e$, $\mathbf{S}_m$, $\mathbf{S}_{rs}$ correspond to the expectation values of the operators $\hat{\boldsymbol{\lambda}}_e$, $\hat{\boldsymbol{\lambda}}_m$, $U^\dagger\hat{\boldsymbol{\lambda}}_{rs}U$. Equation (S5) validate the geometric description of the bispinor polarization state on the Poincaré hypersphere.

II. Total spin density of paraxial waves

The total spin density of the 4D wavefunction $\boldsymbol{\Psi} = [\mathbf{E}, i\mathbf{H}]^T$ is given by the local expectation value of the spin operator:

$$\mathbf{s} = \frac{1}{16\pi\omega} \boldsymbol{\Psi}^\dagger \cdot (\mathbf{J}_2 \otimes \hat{\mathbf{S}}) \boldsymbol{\Psi}, \tag{S6}$$

where $\mathbf{J}_2 = \begin{bmatrix} 1 & 1 \\ 1 & 1 \end{bmatrix}$ and $\hat{\mathbf{S}}$ is the spin-1 operator with elements $\hat{S}_x = -i\begin{bmatrix} 0 & 0 & 0 \\ 0 & 0 & 1 \\ 0 & -1 & 0 \end{bmatrix}$, $\hat{S}_y = -i\begin{bmatrix} 0 & 0 & -1 \\ 0 & 0 & 0 \\ 1 & 0 & 0 \end{bmatrix}$,

and $\hat{S}_z = -i\begin{bmatrix} 0 & 1 & 0 \\ -1 & 0 & 0 \\ 0 & 0 & 0 \end{bmatrix}$. For the considered paraxial waves propagating along z direction, the total spin density reduces to

$$\mathbf{s} = \frac{1}{16\pi\omega} \boldsymbol{\Psi}^\dagger \cdot (\mathbf{J}_2 \otimes \hat{S}_z)\boldsymbol{\Psi} = \frac{1}{16\pi\omega}\left[\mathbf{E}^\dagger \cdot (\hat{S}_z)\mathbf{E} + \mathbf{H}^\dagger \cdot (\hat{S}_z)\mathbf{H} + i\mathbf{E}^\dagger \cdot (\hat{S}_z)\mathbf{H} - i\mathbf{H}^\dagger \cdot (\hat{S}_z)\mathbf{E}\right]$$

$$= \frac{1}{16\pi\omega}\{\text{Im}[\mathbf{E}^* \times \mathbf{E}] + \text{Im}[\mathbf{H}^* \times \mathbf{H}] + \text{Re}[\mathbf{E}^* \times \mathbf{H}] - \text{Re}[\mathbf{H}^* \times \mathbf{E}]\} = \mathbf{s}_e + \mathbf{s}_m + \mathbf{s}_{rs}. \tag{S7}$$

Here, $\mathbf{s}_e = \frac{1}{16\pi\omega}\text{Im}[\mathbf{E}^* \times \mathbf{E}]$ and $\mathbf{s}_m = \frac{1}{16\pi\omega}\text{Im}[\mathbf{H}^* \times \mathbf{H}]$ are the electric and magnetic spin densities that constitute the traditional optical spin density. The third term is a new type of spin density related to the real part of the Poynting vector, which is attributed to the temporal rotation of RS field:

$$\mathbf{s}_{rs} = \frac{1}{16\pi\omega}\{\text{Re}[\mathbf{E}^* \times \mathbf{H}] - \text{Re}[\mathbf{H}^* \times \mathbf{E}]\} = \frac{1}{16\pi\omega}\{\text{Im}[\mathbf{F}_1^* \times \mathbf{F}_1] + \text{Im}[\mathbf{F}_2^* \times \mathbf{F}_2]\}. \tag{S8}$$

III. Geometric phase of paraxial waves

We consider an RS polarization state $|F_1\rangle$ on the RS-sphere ($|F_2\rangle$ can be treated similarly):

$$|F_1\rangle = \cos\left(\frac{\theta}{2}\right)|F_1^{+\kappa}\rangle e^{-\frac{i\kappa\phi}{2}} + \sin\left(\frac{\theta}{2}\right)|F_1^{-\kappa}\rangle e^{\frac{i\kappa\phi}{2}}, \tag{S9}$$

where $|F_1^{\pm\kappa}\rangle = \frac{\sqrt{2}}{2}(\hat{\mathbf{e}}_i \pm i\kappa\hat{\mathbf{h}}_j)$ are basis states located at the north/south pole. A cyclic evolution of $|F_1\rangle$ along a path C on the RS-sphere generates the geometric phase $\Phi_{rs} = \iint_C \mathbf{V}(\mathbf{r}) \cdot d\mathbf{a}$, where $\mathbf{r} = (\rho, \theta, \phi)$ denotes the spherical coordinates, $\mathbf{V}(\mathbf{r}) = \nabla_\mathbf{r} \times \mathbf{A}(\mathbf{r})$ is the Berry curvature with $\mathbf{A}(\mathbf{r}) = i\langle F_1(\mathbf{r})|\nabla_\mathbf{r}|F_1(\mathbf{r})\rangle$ being the Berry connection, and the integral is carried out over the area enclosed by the path C. The Berry connection $\mathbf{A}(\mathbf{r})$ has the following components[1]:

$$A_\rho = i\langle F_1|\partial_\rho|F_1\rangle, \tag{S10}$$

$$A_\theta = i\langle F_1 | \partial_\theta | F_1 \rangle / \rho, \tag{S11}$$

$$A_\phi = i\langle F_1 | \partial_\phi | F_1 \rangle / (\rho \sin\theta). \tag{S12}$$

Substituting Eq. (S9) into the above equations, we obtain $A_\rho = 0$, $A_\theta = 0$, and $A_\phi = \frac{\kappa \cos\theta}{2\rho \sin\theta}$. Thus, the Berry

connection is $\mathbf{A} = (0, 0, \frac{\kappa \cos\theta}{2\rho \sin})$, and the Berry curvature is $\mathbf{V} = \nabla_\mathbf{r} \times \mathbf{A} = \left(-\frac{\kappa}{2\rho^2}, 0, 0 \right)$. Consequently, the

RS geometric phase can be obtained as

$$\Phi_{rs} = \iint_C \mathbf{V}(\mathbf{r}) \cdot d\mathbf{a} = -\frac{1}{2}\kappa\Omega, \tag{S13}$$

where Ω is the solid angle subtended by the area enclosed by path C. Equation (S13) indicates that the RS geometric phase is proportional to the RS spin κ.

The general 4D polarization evolution of paraxial waves can give rise to both the PB and RS phases. The electric and magnetic polarizations of paraxial waves satisfy $\theta_e = \theta_m$ and $\phi_e = \phi_m$. The corresponding 4D polarization state on the Poincaré hypersphere can be expressed as:

$$|\Psi\rangle = \begin{bmatrix} \frac{1}{\sqrt{2}}\left[\cos\left(\frac{\theta_{rs}}{2}\right)e^{-\frac{i\kappa\phi_{rs}}{2}} + \sin\left(\frac{\theta_{rs}}{2}\right)e^{\frac{i\kappa\phi_{rs}}{2}}\right] & \begin{bmatrix}\cos(\frac{\theta_e}{2})e^{-\frac{i\sigma\phi_e}{2}} \\ \sin(\frac{\theta_e}{2})e^{\frac{i\sigma\phi_e}{2}}\end{bmatrix} \\ i\kappa\frac{1}{\sqrt{2}}\left[\cos\left(\frac{\theta_{rs}}{2}\right)e^{-\frac{i\kappa\phi_{rs}}{2}} - \sin\left(\frac{\theta_{rs}}{2}\right)e^{\frac{i\kappa\phi_{rs}}{2}}\right] & \begin{bmatrix}\cos(\frac{\theta_e}{2})e^{-\frac{i\sigma\ e}{2}} \\ \sin(\frac{\theta_e}{2})e^{\frac{i\sigma\phi_e}{2}}\end{bmatrix} \end{bmatrix}\begin{bmatrix}|E_\sigma\rangle \\ |E_{-\sigma}\rangle \\ |H_\sigma\rangle \\ |H_{-\sigma}\rangle\end{bmatrix}, \tag{S14}$$

where $|E_{\pm\sigma}\rangle = \frac{1}{\sqrt{2}}\left(\hat{\mathbf{e}}_i \pm i\sigma\hat{\mathbf{e}}_j\right)$ and $|H_{\pm\sigma}\rangle = \frac{1}{\sqrt{2}}\left(\hat{\mathbf{h}}_j \mp i\sigma\hat{\mathbf{h}}_i\right)$. The total geometric phase induced by the evolution of $|\Psi\rangle$ can be obtained via nesting the E-sphere and H-sphere into the RS-sphere. The electric polarization evolution traces out a path C_e on the E-sphere, while the magnetic polarization evolution traces out a path C_m on the H-sphere. Since $C_e = C_m$ for paraxial waves, we obtain the PB phases $\Phi_e(C_e) = \Phi_m(C_m) = -\frac{1}{2}\sigma\Omega_e$, where σ is the optical spin and Ω_e is the solid angle enclosed by the path C_e. These PB phases manifest in the basis states of the RS-sphere. Meanwhile, the cyclic evolution of the RS polarization over a path C_{rs} on the RS-sphere induces the RS phase $\Phi_{rs}(C_{rs}) = -\frac{1}{2}\kappa\Omega_{rs}$ (see Eq. (S13)), irrespective of the PB phases in the basis states. Thus, the total geometric phase due to the 4D polarization evolution equals the sum of the PB and RS phases:

$$\Phi_{tot} = -\frac{1}{2}\sigma\Omega_e - \frac{1}{2}\kappa\Omega_{rs}. \tag{S15}$$

Equation (S15) reveals that the total geometric phase of paraxial waves arises from the synergy of electric (magnetic) polarization evolution and RS polarization evolution, depending on the optical spin σ and RS spin κ.

For the polarization evolutions induced by the metasurface in Fig. 4 of the main text, we have $\theta_e = \theta_m = \theta_{rs}$ and $\phi_e = \phi_m = \phi_{rs}$, and Eq. (S14) reduces to

$$|\Psi\rangle = \begin{bmatrix} \frac{1}{\sqrt{2}}\left[\cos\left(\frac{\theta}{2}\right)e^{-\frac{i\kappa\phi}{2}} + \sin\left(\frac{\theta}{2}\right)e^{\frac{i\kappa}{2}}\right] & \begin{bmatrix}\cos\left(\frac{\theta}{2}\right)e^{-\frac{i\sigma\phi}{2}} \\ \sin\left(\frac{\theta}{2}\right)e^{\frac{i\sigma\phi}{2}}\end{bmatrix} \\ i\kappa\frac{1}{\sqrt{2}}\left[\cos\left(\frac{\theta}{2}\right)e^{-\frac{i\kappa\phi}{2}} - \sin\left(\frac{\theta}{2}\right)e^{\frac{i\kappa}{2}}\right] & \begin{bmatrix}\cos\left(\frac{\theta}{2}\right)e^{-\frac{i\sigma\phi}{2}} \\ \sin\left(\frac{\theta}{2}\right)e^{\frac{i\sigma}{2}}\end{bmatrix} \end{bmatrix} \begin{bmatrix} |E_\sigma\rangle \\ |E_{-\sigma}\rangle \\ |H_\sigma\rangle \\ |H_{-\sigma}\rangle \end{bmatrix}, \tag{S16}$$

The electric, magnetic, and RS polarization states undergo the same evolution trajectory ($C_e = C_m = C_{rs} = C$), leading to $\Omega_e = \Omega_m = \Omega_{rs} = \Omega$. In this case, the total geometric phase can be explicitly derived using the Berry connection $\mathbf{A}$ based on the Poincaré hyperspheres, which has the following components

$$A_\rho = i\langle\Psi|\partial_\rho|\Psi\rangle, \tag{S17}$$

$$A_\theta = i\langle\Psi|\partial_\theta|\Psi\rangle/\rho, \tag{S18}$$

$$A_\phi = i\langle\Psi|\partial_\phi|\Psi\rangle/(\rho\sin\theta). \tag{S19}$$

Substituting Eq. (S16) into the above equations, we obtain $\mathbf{A} = (0,0,\frac{(\sigma+\kappa)\cos\theta}{2\rho\sin\theta})$. The corresponding Berry curvature is $\mathbf{V} = (-\frac{\sigma+\kappa}{2\rho^2},0,0)$. Thus, the total geometric phase is:

$$\Phi_{\text{tot}} = \iint_C \mathbf{V}(\mathbf{r})\cdot d\mathbf{a} = -\frac{1}{2}(\sigma+\kappa)\Omega, \tag{S20}$$

which corresponds to a special case of Eq. (S15) and indicates that the total geometric phase is proportional to the total spin $s = \sigma + \kappa$.

IV.   Relation between RS phase and reflection/transmission phase

In Fig. 2 of the main text, we have considered the interface separating air and metal, where we show that the RS phase is equal to the reflection/transmission phase predicted by Fresnel equations. We now prove this relationship for a general interface between air and isotropic medium (ε, μ). As shown in Fig. 2(b), the wave transmission and reflection lead to the evolutions of the RS polarization $|F_1^{\text{in}}\rangle \to |F_1^{\text{tra}}\rangle$ and $|F_1^{\text{in}}\rangle \to |F_1^{\text{tra}}\rangle \to |F_1^{\text{ref}}\rangle$, respectively, on the RS-sphere. The Stokes vectors of the states $|F_1^{\text{in}}\rangle$, $|F_1^{\text{tra}}\rangle$, and $|F_1^{\text{ref}}\rangle$ are

$\mathbf{A} = (0,0,1)$, $\mathbf{B} = \left(\frac{1-\frac{|\varepsilon|}{|\mu|}}{1+\frac{|\varepsilon|}{|\mu|}}, \frac{-2\text{Im}\left(\frac{\sqrt{\varepsilon}}{\sqrt{\mu}}\right)}{1+\frac{|\varepsilon|}{|\mu|}}, \frac{2\text{Re}\left(\frac{\sqrt{\varepsilon}}{\sqrt{\mu}}\right)}{1+\frac{|\varepsilon|}{|\mu|}}\right)$, and $\mathbf{C} = (0,0,-1)$, respectively. Then, we can define closed evolution paths $AOBA$ ($AOCBA$) for the transmission (reflection) by choosing the reference point $\mathbf{O} = (1,0,0)$ with the state $\mathbf{F}_1 = \hat{\mathbf{e}}_x$. The corresponding solid angle and geometric phase can be determined as[2]

$$\Phi_{\text{tra}} = \frac{1}{2}\Omega_{AOBA} = \text{atan}\left[\frac{\mathbf{A}\cdot(\mathbf{O}\times\mathbf{B})}{1+\mathbf{O}\cdot\mathbf{B}+\mathbf{A}\cdot\mathbf{B}+\mathbf{A}\cdot\mathbf{O}}\right] = -\text{atan}\left[\frac{\text{Im}\left(\frac{\sqrt{\varepsilon}}{\sqrt{\mu}}\right)}{1+\text{Re}\left(\frac{\sqrt{\varepsilon}}{\sqrt{\mu}}\right)}\right],$$

$$\Phi_{\text{ref}} = \frac{1}{2}\Omega_{AOCBA} = \frac{1}{2}(\Omega_{AOB}+\Omega_{OCB})$$

$$= \text{atan}\left[\frac{\mathbf{A}\cdot(\mathbf{O}\times\mathbf{B})}{1+\mathbf{O}\cdot\mathbf{B}+\mathbf{A}\cdot\mathbf{B}+\mathbf{A}\cdot\mathbf{O}}\right] + \text{atan}\left[\frac{\mathbf{O}\cdot(\mathbf{C}\times\mathbf{B})}{1+\mathbf{C}\cdot\mathbf{B}+\mathbf{O}\cdot\mathbf{B}+\mathbf{O}\cdot\mathbf{C}}\right] = \text{atan}\left[\frac{-\text{Im}\left(\frac{\sqrt{\varepsilon}}{\sqrt{\mu}}\right)}{1+\text{Re}\left(\frac{\sqrt{\varepsilon}}{\sqrt{\mu}}\right)}\right] - \text{atan}\left[\frac{\text{Im}\left(\frac{\sqrt{\varepsilon}}{\sqrt{\mu}}\right)}{1-\text{Re}\left(\frac{\sqrt{\varepsilon}}{\sqrt{\mu}}\right)}\right]. \tag{S21}$$
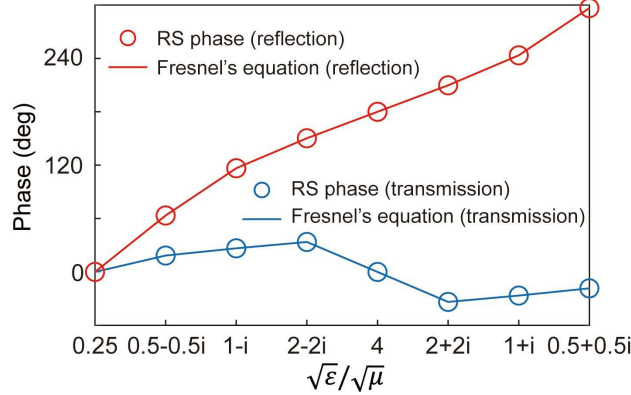
Based on the Fresnel equations, the transmission and reflection coefficients under the normal incidence are

$t = \dfrac{2}{1+\frac{\sqrt{\varepsilon}}{\sqrt{\mu}}}$ and $r = \dfrac{1-\frac{\sqrt{\varepsilon}}{\sqrt{\mu}}}{1+\frac{\sqrt{\varepsilon}}{\sqrt{\mu}}}$. Thus, the transmission and reflection phases are

$$\text{Arg}(t) = -\text{atan}\left[\frac{\text{Im}\left(\frac{\sqrt{\varepsilon}}{\sqrt{\mu}}\right)}{1+\text{Re}\left(\frac{\sqrt{\varepsilon}}{\sqrt{\mu}}\right)}\right], \quad \text{Arg}(r) = \text{atan}\left[\frac{-\text{I}\ \left(\frac{\sqrt{\varepsilon}}{\sqrt{\mu}}\right)}{1-\text{Re}\left(\frac{\sqrt{\varepsilon}}{\sqrt{\mu}}\right)}\right] - \text{atan}\left[\frac{\text{Im}\left(\frac{\sqrt{\varepsilon}}{\sqrt{\mu}}\right)}{1+\text{Re}\left(\frac{\sqrt{\varepsilon}}{\sqrt{\mu}}\right)}\right]. \tag{S22}$$

Equations (S21) and (S22) agree with each other. Thus, the reflection and transmission phases are equal to the RS phases. We further verify the above result by setting $\frac{\sqrt{\varepsilon}}{\sqrt{\mu}} = 0.25, 0.5 - 0.5i, 1 - i, 2 - 2i, 4, 2 + 2i, 1 + i, 0.5 + 0.5i$ and compare the phases obtained with Eqs. (S21) and (S22). The results are shown in Fig. S2. We notice that the RS phases exhibit great consistency with the phase results by Fresnel equations.

Fig. S2 Comparison between the RS geometric phase (symbols) and the reflection/transmission phase (lines) predicted by the Fresnel equations, for wave transmission and reflection at the interface between air and an isotropic medium (ε, μ).

V.   Electric and magnetic responses of the meta-atoms

The local electric and magnetic responses of the meta-atoms in the RS metasurface of Fig. 3(a) can be characterized by the polarizability matrix. The induced electric dipole **p** and magnetic dipole **m** of the bi-anisotropic split ring can be expressed as

$$\begin{bmatrix} \mathbf{p} \\ \mathbf{m} \end{bmatrix} = \begin{bmatrix} \overleftrightarrow{\chi}_{ee} & i\overleftrightarrow{\chi}_{em} \\ -i\overleftrightarrow{\chi}_{em} & \overleftrightarrow{\chi}_{mm} \end{bmatrix} \begin{bmatrix} \mathbf{E} \\ \mathbf{H} \end{bmatrix}, \tag{S23}$$

where **E** (**H**) is the incident electric (magnetic) field, $\overleftrightarrow{\chi}_{ee}$ ($\overleftrightarrow{\chi}_{mm}$) is the electric (magnetic) polarizability tensor, and $\overleftrightarrow{\chi}_{em}$ is the magnetoelectric polarizability tensor. Here, the incidence is a plane wave with linearly polarized electric and magnetic fields, of which the RS field can be written as $\mathbf{F}_1^{in} = \left(E\hat{\mathbf{e}}_x + iH\hat{\mathbf{h}}_y\right)e^{i\kappa_{in}k_0 z - i\omega t} = \left(\hat{\mathbf{e}}_x + i\kappa_{in}\hat{\mathbf{h}}_y\right)Ee^{i\kappa_{in}k_0 z - i\omega t}$. In the subwavelength regime, the fundamental eigenmode of the split ring is dominantly excited, and Eq. (S23) simplifies to

$$\begin{bmatrix} p_x \\ m_y \end{bmatrix} = \begin{bmatrix} \chi_{ee}^{xx} & i\chi_{em}^{xy} \\ -i\chi_{em}^{xy} & \chi_{mm}^{yy} \end{bmatrix} \begin{bmatrix} E_x \\ H_y \end{bmatrix}. \tag{S24}$$

Thus, the split ring gives rise to the RS dipole $\mathbf{D}_{rs} = p_x\hat{\mathbf{e}}_x + im_y\hat{\mathbf{h}}_y$. The orientation angle of $\mathbf{D}_{rs}$ in the constitutive frame is

$$\alpha_{\rm rs} = \tan^{-1}\left(\frac{im_y}{p_x}\right). \tag{S25}$$

In the main text, we rotate the split ring around the x/y axis to vary $\alpha_{\rm rs}$. Here, we provide a detailed theoretical derivation for the relationship between $\alpha_{\rm rs}$ and the spatial rotations around x/y axis. We denote the polarizability matrix of the unrotated split ring as M, which has the following elements

$$M = \begin{bmatrix} \vec{\overrightarrow{\chi}}_{\rm ee} & i\vec{\overrightarrow{\chi}}_{\rm em} \\ -i\vec{\overrightarrow{\chi}}_{\rm em} & \vec{\overrightarrow{\chi}}_{\rm mm} \end{bmatrix} = \begin{bmatrix} \chi_{\rm ee}^{xx} & 0 & 0 & 0 & i\chi_{\rm em}^{xy} & 0 \\ 0 & 0 & 0 & 0 & 0 & 0 \\ 0 & 0 & 0 & 0 & 0 & 0 \\ 0 & 0 & 0 & 0 & 0 & 0 \\ -i\chi_{\rm em}^{xy} & 0 & 0 & 0 & \chi_{\rm mm}^{yy} & 0 \\ 0 & 0 & 0 & 0 & 0 & 0 \end{bmatrix}. \tag{S26}$$

The polarizability elements satisfy $\frac{\chi_{\rm em}^{xy}}{\chi_{\rm ee}^{xx}} = \frac{\chi_{\rm mm}^{yy}}{\chi_{\rm em}^{xy}}$. Consequently, the electric and magnetic dipoles have the fixed eigen-relation $|p_x|/|m_y| = |\chi_{\rm em}^{xy}|/|\chi_{\rm ee}^{xx}|$ and $\mathrm{Arg}(p_x) - \mathrm{Arg}(m_y) = \pm\frac{\pi}{2}$.

Rotating the meta-atom by angle α_x around the x-axis leads to the transformation $M' = \widehat{\mathbb{R}'}(\alpha_x)M\widehat{\mathbb{R}'}(-\alpha_x)$, where $\widehat{\mathbb{R}'}(\alpha_x) = \begin{bmatrix} \widehat{\mathbb{R}}(\alpha_x) & 0 \\ 0 & \widehat{\mathbb{R}}(\alpha_x) \end{bmatrix}$ and $\widehat{\mathbb{R}}(\alpha_x) = \begin{bmatrix} 1 & 0 & 0 \\ 0 & \cos\alpha_x & -\sin\alpha_x \\ 0 & \sin\alpha_x & \cos\alpha_x \end{bmatrix}$ is the rotation operator. The transformed polarizability matrix is

$$M' = \begin{bmatrix} \chi_{\rm ee}^{xx} & 0 & 0 & 0 & i\chi_{\rm em}^{xy}\cos\alpha_x & -i\chi_{\rm em}^{xy}\sin\alpha_x \\ 0 & 0 & 0 & 0 & 0 & 0 \\ 0 & 0 & 0 & 0 & 0 & 0 \\ 0 & 0 & 0 & 0 & 0 & 0 \\ -i\chi_{\rm em}^{xy}\cos\alpha_x & 0 & 0 & 0 & \chi_{\rm mm}^{yy}\cos^2\alpha_x & \chi_{\rm mm}^{yy}\cos\alpha_x\sin\alpha_x \\ i\chi_{\rm em}^{xy}\sin\alpha_x & 0 & 0 & 0 & -\chi_{\rm mm}^{yy}\cos\alpha_x\sin\alpha_x & \chi_{\rm mm}^{yy}\sin^2\alpha_x \end{bmatrix}. \tag{S27}$$

Under the normal incidence of a plane wave, only p_x and m_y of the split ring will couple to the output channels. Thus, the effective polarizability matrix in the local constitutive frame $(\hat{\mathbf{e}}_x, \hat{\mathbf{h}}_y)$ is

$$M'_{\rm eff} = \begin{bmatrix} \chi_{\rm ee}^{xx} & i\chi_{\rm em}^{xy}\cos\alpha_x \\ -i\chi_{\rm em}^{xy}\cos\alpha_x & \chi_{\rm mm}^{yy}\cos^2\alpha_x \end{bmatrix}. \tag{S28}$$

It is clear that the rotation $\widehat{\mathbb{R}'}(\alpha_x)$ reduces the magnetoelectric coupling and the magnetic response. Specially, the x-direction electric dipole dominates when $\alpha_x = 90$ deg. Generally, the induced electric dipole p_x and magnetic dipole m_y at the rotation angle α_x are:

$$\begin{bmatrix} p_x \\ m_y \end{bmatrix} = M'_{\rm eff}\begin{bmatrix} E_x \\ H_y \end{bmatrix} \propto \begin{bmatrix} \chi_{\rm ee}^{xx} \\ -i\chi_{\rm em}^{xy}\cos\alpha_x \end{bmatrix} e^{i\kappa\tan^{-1}\left(\frac{\chi_{\rm em}^{xy}\cos\alpha_x}{\chi_{\rm ee}^{xx}}\right)}. \tag{S29}$$

We notice that the relative phase of p_x and m_y is fixed at $\pi/2$, which is protected by the magnetoelectric coupling of the meta-atom. Thus, the RS dipole $\mathbf{D}_{\rm rs}$ lies on the equator of the RS-sphere. In addition, the relative amplitude of p_x and m_y can be controlled by tuning α_x. Substituting Eq. (S29) into Eq. (S25), we obtain

$$\alpha_{\rm rs} = \tan^{-1}\left(\frac{im_y}{p_x}\right) = \tan^{-1}\left(\frac{\chi_{\rm em}^{xy}\cos\alpha_x}{\chi_{\rm ee}^{xx}}\right), \tag{S30}$$

which indicates that the orientation of the local constitutive frame can be controlled with α_x. Finally, we point out that the excitation phase of $\mathbf{D}_{rs}$, i.e., $\kappa \tan^{-1}\left(\frac{\chi_{em}^{xy}\cos{\alpha_x}}{\chi_{ee}^{xx}}\right)$ in Eq. (S29), can be understood as the RS geometric phase arising from the coupling of RS spin with the rotation of the local constitutive frame.

The x-axis rotation only gives rise to the limited range of $\alpha_{rs} \in \left[-\tan^{-1}\left(\frac{\chi_{em}^{xy}}{\chi_{ee}^{xx}}\right), \tan^{-1}\left(\frac{\chi_{em}^{xy}}{\chi_{ee}^{xx}}\right)\right]$. To achieve the full range $\alpha_{rs} \in [-90°, 90°]$, we introduce the y-axis rotation $\widehat{\mathbb{R}^r}(\alpha_y) = \begin{bmatrix} \mathbb{R}(\alpha_y) & 0 \\ 0 & \widehat{\mathbb{R}}(\alpha_y) \end{bmatrix}$ with

$$\widehat{\mathbb{R}}(\alpha_y) = \begin{bmatrix} \cos\alpha_y & 0 & \sin\alpha_y \\ 0 & 1 & 0 \\ -\sin\alpha_y & 0 & \cos\alpha_y \end{bmatrix}$$, which transforms the polarizability matrix in a similar way:

$$M' = \widehat{\mathbb{R}^r}(\alpha_y) M \widehat{\mathbb{R}^r}(-\alpha_y) = \begin{bmatrix} \chi_{ee}^{xx}\cos^2\alpha_y & 0 & -\chi_{ee}^{xx}\cos\alpha_y\sin\alpha_y & 0 & i\chi_{em}^{xy}\cos\alpha_y & 0 \\ 0 & 0 & 0 & 0 & 0 & 0 \\ -\chi_{ee}^{xx}\cos\alpha_y\sin\alpha_y & 0 & \chi_{ee}^{xx}\sin^2\alpha_y & 0 & -i\chi_{em}^{xy}\sin\alpha_y & 0 \\ 0 & 0 & 0 & 0 & 0 & 0 \\ -i\chi_{em}^{xy}\cos\alpha_y & 0 & i\chi_{em}^{xy}\sin\alpha_y & 0 & \chi_{mm}^{yy} & 0 \\ 0 & 0 & 0 & 0 & 0 & 0 \end{bmatrix} \quad \text{(S31)}$$

Differently, the $\widehat{\mathbb{R}^r}(\alpha_y)$ rotation reduces the magnetoelectric coupling and the electric response. The y-direction magnetic dipole dominates at $\alpha_y = 90$ deg. Generally, the induced electric dipole p_x and magnetic dipole m_y can be expressed as

$$\begin{bmatrix} p_x \\ m_y \end{bmatrix} = M'_{2D} \begin{bmatrix} E_x \\ H_y \end{bmatrix} \propto \begin{bmatrix} \chi_{ee}^{xx}\cos\alpha_y \\ -i\chi_{em}^{xy} \end{bmatrix} e^{i\kappa\tan^{-1}\left(\frac{\chi_{em}^{xy}}{\chi_{ee}^{xx}\cos\alpha_y}\right)}. \quad \text{(S32)}$$

The orientation angle of the RS dipole $\mathbf{D}_{rs}$ is

$$\alpha_{rs} = \tan^{-1}\left(\frac{im_y}{p_x}\right) = \tan^{-1}\left(\frac{\chi_{em}^{xy}}{\chi_{ee}^{xx}\cos\alpha_y}\right), \quad \text{(S33)}$$

which takes values within the range $[-90, -\tan^{-1}\left(\frac{\chi_{em}^{xy}}{\chi_{ee}^{xx}}\right)]$ and $[\tan^{-1}\left(\frac{\chi_{em}^{xy}}{\chi_{ee}^{xx}}\right), 90]$.

The meta-atom rotations around x-axis and y-axis together realize the free rotation of the RS dipole and thus the RS phase with 2π full range. In Fig. S3, we show the simulation and analytical (based on Eqs. (S30) and (S33)) results of α_{rs} for the rotation angles $\alpha_x \in [0,180]$ and $\alpha_y \in [-180,0]$, which show great consistency with each other.
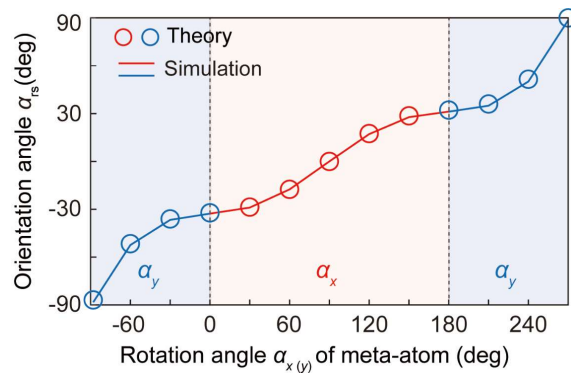
Fig. S3 The analytical (circle) and simulation (solid line) results for the orientation angle of the RS dipole induced by the meta-atom rotations around x-axis (red region) and y-axis (blue region).

VI.   Dependence of RS phase on incident direction

In the system of Fig. 3(a) in the main text, we have assumed the plane wave incident along -z direction with RS spin $\kappa_{in} = -1$. If the propagation direction of the incident wave is flipped so that $\kappa_{in} = 1$, as shown in Fig. S4(a), the RS metasurface will induce different RS polarization evolutions $|+1\rangle \rightarrow |+1\rangle$ and $|+1\rangle \rightarrow |-1\rangle$, leading to different deflections of scattering fields compared with those in Fig. 3. We note that the polarization of the RS dipole induced in the meta-atom is not influenced by the flipping of propagation direction. Figure S4(b) shows the RS polarization evolution on the RS-sphere. The RS polarization evolution $|F_1^{in}\rangle \rightarrow |D_{rs}\rangle \rightarrow |F_1^{out}\rangle$ for the backward scattering field gives rise to the RS phase $2\alpha_{rs}$, which is opposite to the RS phase in Fig. 3 due to the flipping of incident RS spin κ_{in}. Meanwhile, the polarization evolution $|F_1^{in}\rangle \rightarrow |D_{rs}\rangle \rightarrow |F_1^{out}\rangle$ for the forward scattering field exbibits no geometric phase. To validate the theoretical picture, we compare the geometric phase (circles) and simulated phase (solid lines) of the forward/backward scatterings in Fig. S4(c) for different orientation angles of the RS dipole, which show great consistency with each other. In addition, the forward/backward scattering amplitude remains approximately constant for different orientation angles. Figure S4(d) shows the simulated scattering fields of the metasurface, where the forward scattering exhibits no deflection while the backward scattering is deflected due to the RS geometric phase gradient.
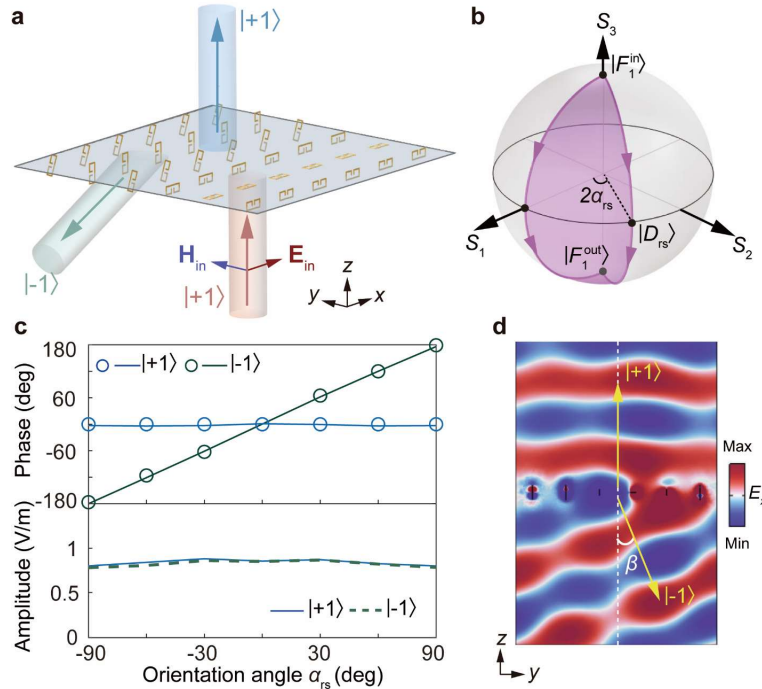

Fig. S4 (a) Schematic of RS metasurface under the incidence of the linearly polarized plane wave propagating along the $+z$ direction. (b) RS polarization evolution on the RS-sphere. (c) RS phase, simulated phase, and simulated amplitude of the scattering fields for different α_{rs}. (d) Simulated scattering fields E_x by the metasurface.

## VII. Dependence of total geometric phase on incident electric spin

In the system of Fig. 4(a), we assume the electric and magnetic fields of the incident plane wave are LCP. Here, to increase the wavefront channels, we further provide simulation results for the incident plane wave with RCP electric and magnetic fields, corresponding to flipping the optical spin $\sigma_{in} = -1 \rightarrow \sigma_{in} = +1$, as shown in Fig. S5(a). In this case, the total spin of the incident wave is $s_{inc} = \sigma + \kappa = 0$. The corresponding four polarization evolution channels are: $|+1,-1\rangle \rightarrow |+1,-1\rangle$, $|+1,-1\rangle \rightarrow |-1,-1\rangle$, $|+1,-1\rangle \rightarrow |+1,+1\rangle$, and $|+1,-1\rangle \rightarrow |-1,+1\rangle$, which give rise to different geometric phases and wavefronts compared to Fig. 4(a). Specifically, the outputs $|-1,-1\rangle$ and $|+1,+1\rangle$ are deflected along opposite directions, while $|-1,+1\rangle$ and $|+1,-1\rangle$ exbibit no deflection. For the $|+1,-1\rangle \rightarrow |-1,+1\rangle$ channel, electric (magnetic) polarization and RS polarization undergo opposite evolutions, as shown in Fig. S5(b). Thus, the PB and RS phases cancel each other, resulting in zero total geometric phases, which is consistent with the simulated results in Fig. S5(c). For the channel $|+1,-1\rangle \rightarrow |+1,+1\rangle$ ($|+1,-1\rangle \rightarrow |-1,-1\rangle$), the flipping of only RS (electric) spin results in the total geometric phase $\Phi_{tot} = (\kappa_{in} - \kappa_{out})\alpha_{rs} = -2\alpha_{rs}$ [$\Phi_{tot} = (\sigma_{in} - \sigma_{out})\alpha_e = 2\alpha_e$], which is also consistent with the simulation results in Fig. S5(c). In Fig. S5(d), we show that the amplitudes of four channels, which vary slightly with the orientation angle of the RS dipole in the meta-atom. In Fig. S5(e), the left panel shows the normal propagation of $|-1,+1\rangle$ and deflection of $|-1,-1\rangle$ along the y direction ($\beta = 22.3$ deg); the right panel exhibits the deflection of $|+1,+1\rangle$ along the $-y$ direction ($\beta = 22.3$ deg) and normal propagation of $|+1,-1\rangle$.
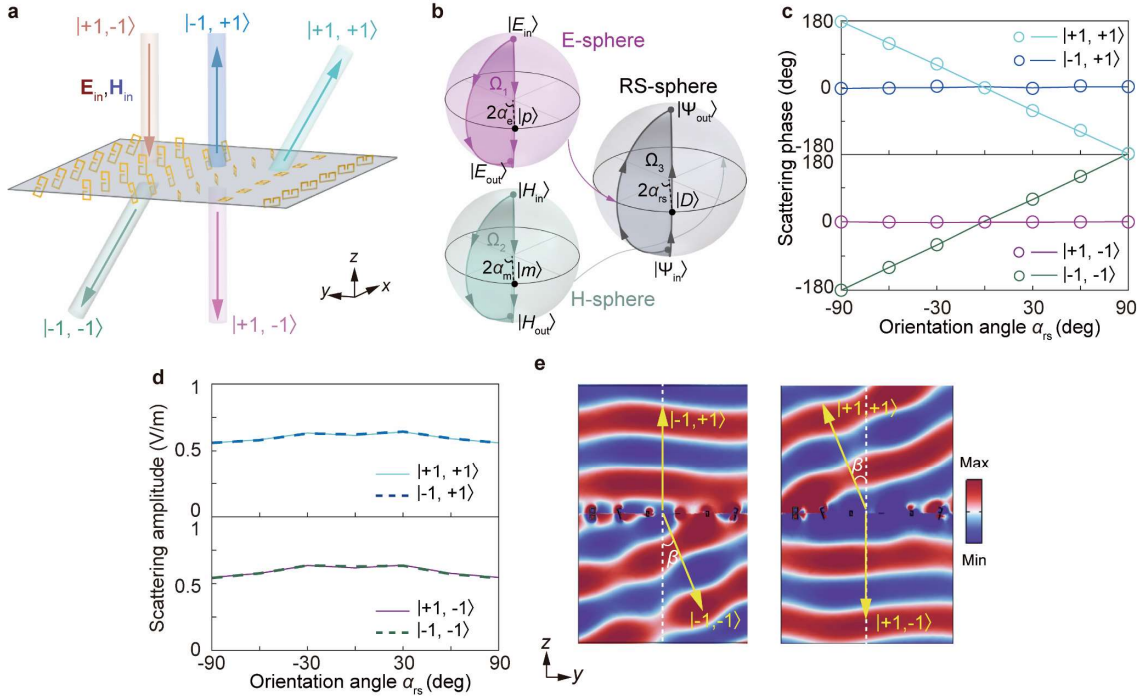
Fig. S5 (a) Higher-order RS metasurface under the incidence of the plane wave with RCP electric and magnetic fields. (b) 4D polarization evolution on the Poincaré hypersphere. (c) Phases and (d) amplitudes of the four scattering channels as a function of the orientation angle α_{rs} of the RS dipole in the meta-atom. (e) Simulated scattering fields of the four channels.

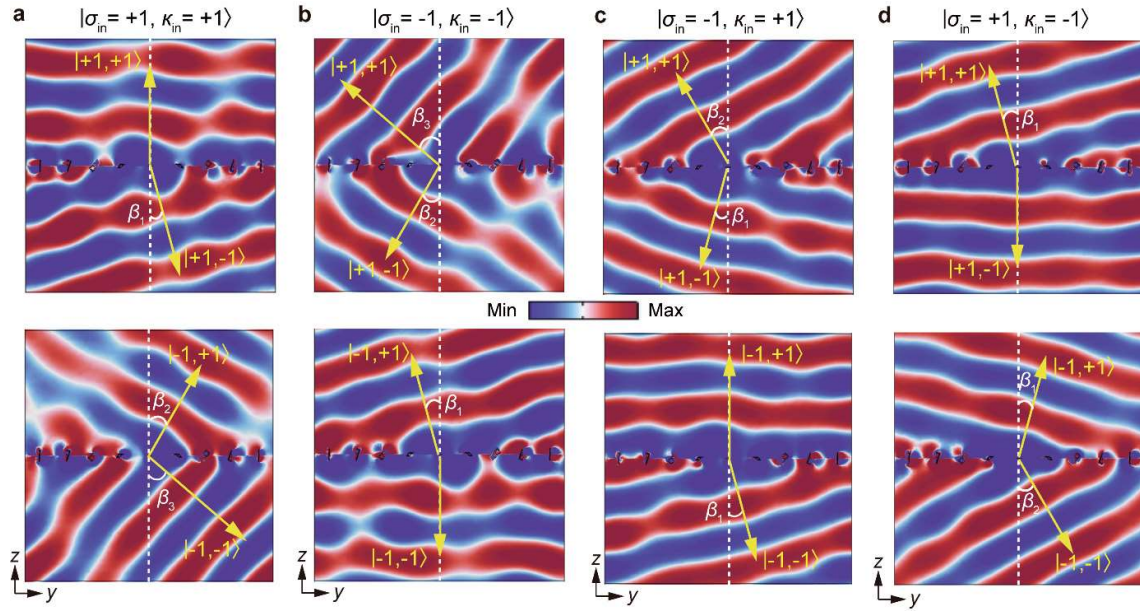## VIII. High-dimensional multiplexed steering

In Fig. 4 and Fig. S5, we have shown the wavefronts generated by the high-order RS metasurface with $\alpha_p = \alpha_m = \alpha_{rs}$ under the incidence of the plane waves $|\sigma_{in} = \pm 1, \kappa_{in} = -1\rangle$. The metasurface can further generate different wavefronts if the RS spin of incident wave is flipped ($\kappa_{in} = -1 \rightarrow \kappa_{in} = +1$), corresponding to the incident plane waves $|\sigma_{in} = \pm 1, \kappa_{in} = +1\rangle$. In total, the metasurface can give rise to eight distinct wavefronts, as schematically depicted in Fig. S6(a). Figures S6(b) shows the simulated output wavefronts for the incident plane wave with $|\sigma_{in} = +1, \kappa_{in} = +1\rangle$. The output wave $|-1, -1\rangle$ is deflected along the y direction with the largest angle $\beta_2 = 49$ deg, the output waves $|-1, +1\rangle$ and $|+1, -1\rangle$ are deflected with the same angle $\beta_1 = 23$ deg, while the output wave $|+1, +1\rangle$ shows no deflection. Figures S6(c) shows the simulated output wavefronts for the incident plane wave with $|\sigma_{in} = -1, \kappa_{in} = +1\rangle$. The output waves $|-1, -1\rangle$ and $|+1, +1\rangle$ are deflected along the opposite direction with the same angle $\beta_1 = 23$ deg, while the output waves $|-1, +1\rangle$ and $|+1, -1\rangle$ exhibit normal propagation. In Fig. S6(d), we show the simulated far-field intensity patterns under the normally incident plane waves with switchable 4D polarization. As seen, a total of eight distinct intensity lobes are generated by the metasurface, labelled in accordance with the numbers in Fig. S6(a).
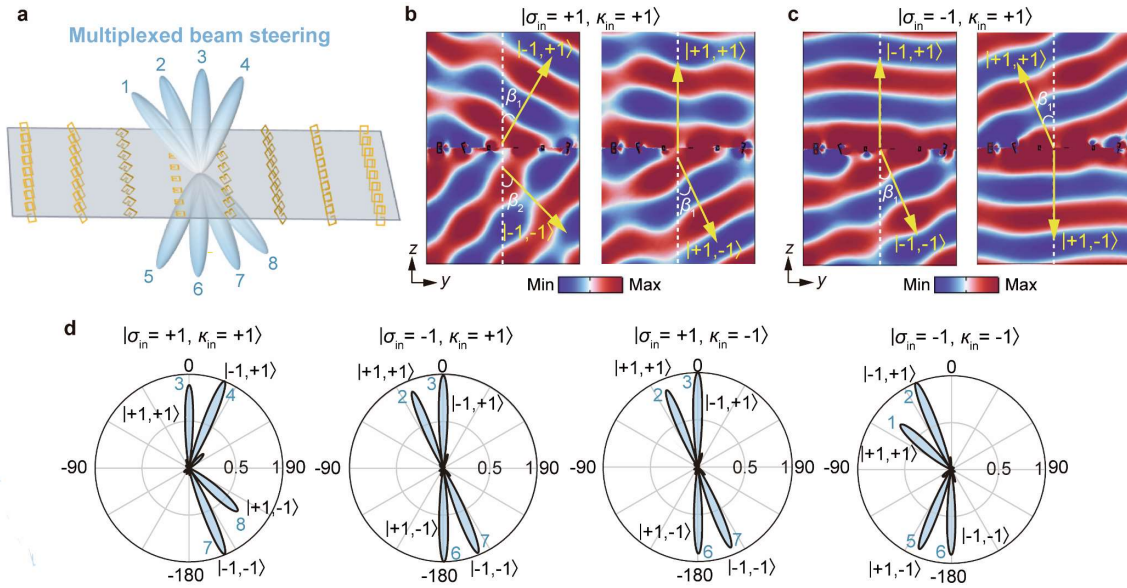
Fig. S6 (a) Schematic of the multiplexed beam steering with eight distinct output wavefronts. Simulated electric field distribution of output waves under the incidence (b) $|\sigma_{in} = +1, \kappa_{in} = +1\rangle$ and (c) $|\sigma_{in} = -1, \kappa_{in} = +1\rangle$. (d) Far-field intensity patterns under four orthogonal incidences.

In Fig. 5 of the main text, we have shown that a general RS metasurface ($\alpha_p = \alpha_m \neq \alpha_{rs}$) with decoupled PB and RS phases can generate a total of twelve far-field intensity lobes in different scattering directions, under the incidence of the plane waves $|\sigma_{in} = \pm 1, \kappa_{in} = \pm 1\rangle$. Here, we plot in Fig. S7 the scattering electric field in each channel to show the multiplexed wavefronts. Specifically, under the incidence $|\sigma_{in} = +1, \kappa_{in} = +1\rangle$, the outputs $|+1, -1\rangle$, $|-1, +1\rangle$, and $|-1, -1\rangle$ are deflected along the y direction

with different angles $\beta_1 = 15$ deg, $\beta_2 = 30$ deg, and $\beta_3 = 49$ deg, while the output $|+1, +1\rangle$ shows no deflection, as shown in Fig. S7(a). Distinctly, under the incidence $|\sigma_{in} = -1, \kappa_{in} = -1\rangle$, the outputs $|-1, +1\rangle$, $|+1, -1\rangle$, and $|+1, +1\rangle$ are deflected along the $-y$ direction with the angle β_1, β_2, and β_3, while the output $|-1, -1\rangle$ exhibits no deflection, as shown in Fig. S7(b). For the incidence $|\sigma_{in} = -1, \kappa_{in} = +1\rangle$ in Fig. S7(c), the outputs $|+1, -1\rangle$ and $|-1, -1\rangle$ are deflected along opposite directions with the same angle β_1; the output $|+1, +1\rangle$ is deflected along the $-y$ direction with the angle β_2, while the output $|-1, +1\rangle$ shows no deflection. For the incidence $|\sigma_{in} = +1, \kappa_{in} = -1\rangle$ in Fig. S7(d), the outputs $|+1, +1\rangle$ and $|-1, +1\rangle$ are deflected along opposite directions with the same angle β_1; the output $|-1, -1\rangle$ is deflected along the y direction with the angle β_2, while the output $|+1, -1\rangle$ shows no deflection. These results are consistent with the far-field intensity patterns in Fig. 5 of the main text.


Fig. S7 High-dimensional multiplexed wavefront manipulation by a general RS metasurface under the normal incidence of the plane waves with (a) $|\sigma_{in} = +1, \kappa_{in} = +1\rangle$ and (b) $|\sigma_{in} = -1, \kappa_{in} = -1\rangle$, (c) $|\sigma_{in} = -1, \kappa_{in} = +1\rangle$, and (d) $|\sigma_{in} = +1, \kappa_{in} = -1\rangle$. The yellow arrows denote the deflection directions of output waves.

IX. Effect of the metasurface substrate

We conduct microwave experiments to verify the theory and demonstrate high-dimensional wavefront manipulation by the RS metasurfaces. The copper split rings are fabricated with PCB on Roger's 5880 substrate and have the geometric parameters: $t_1 \times t_2 = 0.035\ \text{mm} \times 0.15\ \text{mm}$, $h = 0.85\ \text{mm}$, $w = 2.2\ \text{mm}$, $l = 0.48\ \text{mm}$, and $g = 0.428\ \text{mm}$ (see Fig. 3(a) for the definitions of these parameters). Note that these parameters are used in experiments and related simulations [Fig. 3(f) and Fig. 4(f)]; they are slightly different from those used in numerical demonstrations [Fig. 3(c, d) and Fig. 4(c, d)]. In the numerical demonstrations, we did not simulate the substrate. Here, we provide further simulation results to show that the optical functionality of the metasurface is not affected by the substrate.

Figure S8(a) shows the simulated RS metasurface with substrate. The thickness and height of the substrate are $t_s = 0.508$ mm and $h_s = 4$ mm. Figure S8(b) shows the phases and amplitudes of the scattering fields for $\alpha_{rs} = -90, -60, -30, 0, 30, 60,$ and 90 degrees, which exhibit similar properties as those in Fig. 3(c). The split rings corresponding to the seven values of α_{rs} have the following rotation angles $(\alpha_x, \alpha_y, \alpha_z)$ in degrees: (0,−90,0), (0,−75,0), (0,−40,0), (−90,0,0), (0,140,0), (0,105,0), and (0,90,0). The Janus-type wave deflection induced by the metasurface is shown in Fig. S8(c), which is also similar to Fig. 3(d).

We also verify the substrate effect in the higher-order RS metasurface. Figure S9(a) shows the simulated metasurface with substrate. The substrate piece has the dimensions $l_s \times h_s = 4$ mm $\times 4$ mm. Figures S9(b) and S9(c) show the phases and amplitudes of the four scattering waves, which are similar to those in Fig. 4(c) of the main text and exhibit good agreements between the simulation and analytical results. The split rings corresponding to the seven values of $\alpha_{rs} = \alpha_e$ have the following rotation angles $(\alpha_x, \alpha_y, \alpha_z)$ in degrees: (0,−90,−90), (0,−75, −60), (0,−40, −30), (−90,0,0), (0,140,30), (0,105,60), and (0,90,90). The scattering field patterns generated by the metasurface are shown in Fig. S9(d), which are similar to Fig. 4(d). These results demonstrate that the RS metasurfaces with substrate can give rise to the same optical functionality.
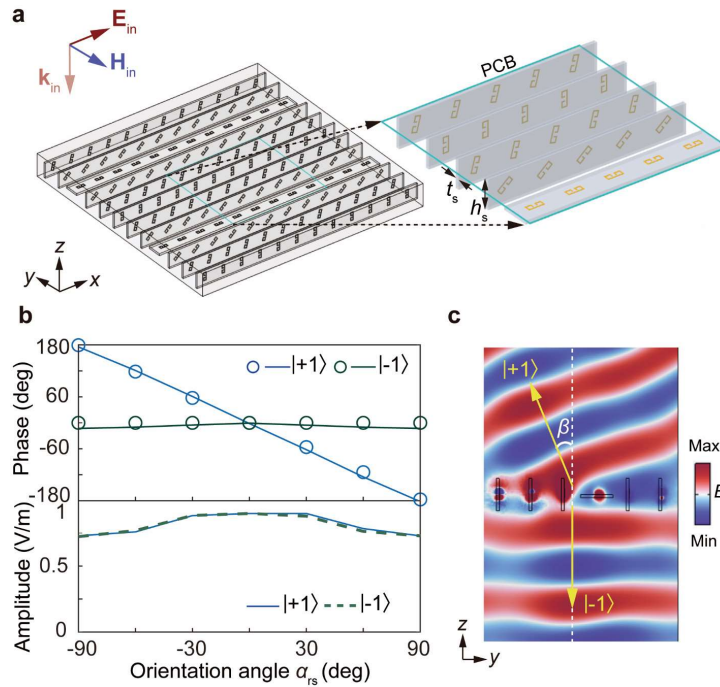
Fig. S8 (a) Simulated RS metasurface with substrate. (b) RS geometric phase (circle), simulated phase (solid line), and field amplitude in two channels. (c) Scattering fields of the metasurface.
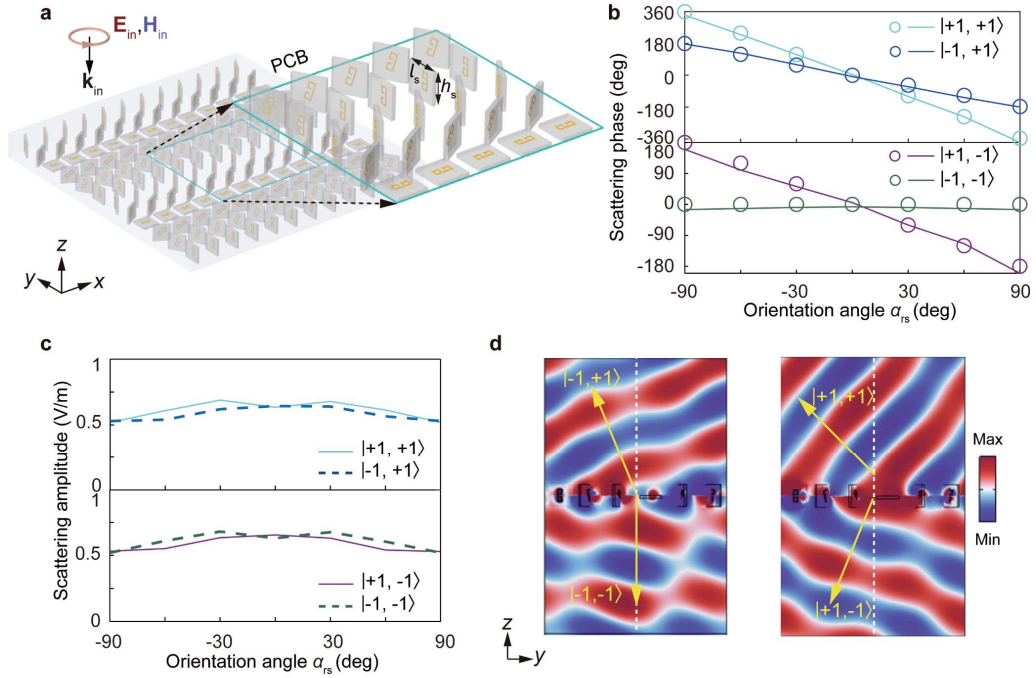
Fig. S9 (a) Simulated higher-order RS metasurface with substrate. (b) RS geometric phase (circle) and simulated phase (solid line) in four channels. (c) Scattering field amplitudes in four channels. (d) Scattering fields of the metasurface.

Reference

1   Berry, M. V. Quantal phase factors accompanying adiabatic changes. *Proc. R. Soc. Lond. A* **392**, 45-57 (1984).

2   van Dijk, T., Schouten, H. F. & Visser, T. D. Geometric interpretation of the Pancharatnam connection and non-cyclic polarization changes. *J. Opt. Soc. Am. A* **27**, 1972-1976 (2010).

3   Pancharatnam, S. Generalized theory of interference, and its applications. *Proc. Indian Acad. Sci. Sect. A* **44**, 247-262 (1956).

4   Samuel, J. & Bhandari, R. General Setting for Berry's phase. *Phys. Rev. Lett.* **60**, 2339-2342 (1988).